

# Proper Motions of Dwarf Spheroidal Galaxies from *Hubble Space Telescope* Imaging. IV: Measurement for Sculptor.<sup>1</sup>

Slawomir Piatek

*Dept. of Physics, New Jersey Institute of Technology, Newark, NJ 07102*  
*E-mail address: piatek@physics.rutgers.edu*

Carlton Pryor

*Dept. of Physics and Astronomy, Rutgers, the State University of New Jersey, 136 Frelinghuysen Rd.,  
 Piscataway, NJ 08854-8019*  
*E-mail address: pryor@physics.rutgers.edu*

Paul Bristow

*Space Telescope European Co-ordinating Facility, Karl-Schwarzschild-Str. 2, D-85748, Garching bei  
 Munchen, Germany*  
*E-mail address: bristowp@eso.org*

Edward W. Olszewski

*Steward Observatory, The University of Arizona, Tucson, AZ 85721*  
*E-mail address: eolszewski@as.arizona.edu*

Hugh C. Harris

*US Naval Observatory, Flagstaff Station, P. O. Box 1149, Flagstaff, AZ 86002-1149*  
*E-mail address: hch@nobs.navy.mil*

Mario Mateo

*Dept. of Astronomy, University of Michigan, 830 Denninonson Building, Ann Arbor, MI 48109-1090*  
*E-mail address: mateo@astro.lsa.umich.edu*

Dante Minniti

*Universidad Catolica de Chile, Department of Astronomy and Astrophysics, Casilla 306, Santiago 22, Chile*  
*E-mail address: dante@astro.puc.cl*

Christopher G. Tinney

*Anglo-Australian Observatory, PO Box 296, Epping, 1710, Australia*  
*E-mail address: cgt@aaoepp.aao.gov.au*

## ABSTRACT

This article presents a measurement of the proper motion of the Sculptor dwarf spheroidal galaxy determined from images taken with the Hubble Space Telescope using the Space Telescope Imaging Spectrograph in the imaging mode. Each of two distinct fields contains a quasi-stellar object which serves as the “reference point.” The measured proper motion of Sculptor, expressed in the equatorial coordinate system, is  $(\mu_\alpha, \mu_\delta) = (9 \pm 13, 2 \pm 13)$  mas century<sup>-1</sup>. Removing the

contributions from the motion of the Sun and the motion of the Local Standard of Rest produces the proper motion in the Galactic-rest-frame:  $(\mu_{\alpha}^{\text{Grf}}, \mu_{\delta}^{\text{Grf}}) = (-23 \pm 13, 45 \pm 13) \text{ mas century}^{-1}$ . The implied space velocity with respect to the Galactic center has a radial component of  $V_r = 79 \pm 6 \text{ km s}^{-1}$  and a tangential component of  $V_t = 198 \pm 50 \text{ km s}^{-1}$ . Integrating the motion of Sculptor in a realistic potential for the Milky Way produces orbital elements. The perigalacticon and apogalacticon are 68 (31, 83) kpc and 122 (97, 313) kpc, respectively, where the values in the parentheses represent the 95% confidence interval derived from Monte Carlo experiments. The eccentricity of the orbit is 0.29 (0.26, 0.60) and the orbital period is 2.2 (1.5, 4.9) Gyr. Sculptor is on a polar orbit around the Milky Way: the angle of inclination is 86 (83, 90) degrees.

*Subject headings:* galaxies: dwarf spheroidal — galaxies: individual (Sculptor) — astrometry: proper motion

## 1. Introduction

Shapley (1938) discovered the Sculptor dwarf spheroidal (dSph) galaxy — the first example of this type of galaxy in the vicinity of the Milky Way — on a plate with a 3 hour exposure time taken with the Bruce telescope. Shapely notes “... that systems such as the Sculptor cluster may not be uncommon; their luminosity characteristics would enable them to escape easy discovery.” Since the detection of Sculptor, astronomers have identified eight other dSphs.

Sculptor is at a celestial location of  $(\alpha, \delta) = (01^{\text{h}}00^{\text{m}}09^{\text{s}}, -33^{\circ}42'30'')$  (J2000.0; Mateo 1998), which corresponds to Galactic coordinates of  $(\ell, b) = (287^{\circ}.5, -83^{\circ}.2)$ . Thus, Sculptor lies nearly at the South Galactic Pole.

Kaluzny et al. (1995) searched for variable stars in a  $15' \times 15'$  field centered approximately on the dSph by taking  $V$ - and  $I$ -band images with the 1-m Swope telescope at Las Campanas Observatory over a period of more than two months. The search resulted in the identification of 226 RR Lyr stars. The average  $V$ -band magnitude of the RR Lyr stars gives a distance modulus of  $(m - M)_V = 19.71$ , which corresponds to a heliocentric distance of 87 kpc. This estimate is practically the same as that obtained by Hodge (1965); it is consistent with the estimate of Baade & Hubble (1939), but somewhat larger than the estimate of Kunkel & Demers (1977). This study adopts the estimate of Kaluzny et al. (1995) for the distance to Sculptor.

Irwin & Hatzidimitriou (1995) derives the most comprehensive set of structural parameters for Sculptor — and seven other dSphs — using star counts from UK Schmidt telescope plates. With a luminosity of  $(1.4 \pm 0.6) \times 10^6 L_{\odot}$ , Sculptor is among the most luminous dSphs. Its major-axis core and limiting radii are  $5.8 \pm 1.6 \text{ arcmin}$  and  $76.5 \pm 5.0 \text{ arcmin}$ , respectively, which are in good agreement with the values derived by Demers, Kunkel, & Krautter (1980). However, they differ from the values derived by Eskridge (1988a), who also uses star counts from UK Schmidt telescope plates. The discrepancy is likely due to an underestimation of the central density in the latter study for reasons that are discussed in Irwin & Hatzidimitriou (1995). The isopleth map of Sculptor (Panel (f) of Figure 1 in Irwin & Hatzidimitriou 1995) shows that the ellipticity of the isodensity contours increases with increasing projected radius from the center of the dSph: the ellipticity is consistent with 0 in the inner 10 arcmin and smoothly increases to a value of 0.32 in the outermost region.

---

<sup>1</sup>Based on observations with NASA/ESA *Hubble Space Telescope*, obtained at the Space Telescope Science Institute, which is operated by the Association of Universities for Research in Astronomy, Inc., under NASA contract NAS 5-26555.

The study observes that Sculptor “... looks remarkably similar to numerical simulations of dSph galaxies that are tidally distorted.” The position angle of the major axis is  $99 \pm 1$  degrees. Eskridge (1988b) finds asymmetric “structure” in Sculptor in an isopleth map of the difference between the stellar surface density and a fitted 2-D model. In contrast, Irwin & Hatzidimitriou (1995) finds only the increase of the ellipticity with projected radius in a similar map. The left panel in Figure 1 shows a  $30 \text{ arcmin} \times 30 \text{ arcmin}$  region of the sky centered on Sculptor. The dashed ellipse is the boundary of the core.

Walcher et al. (2003) studies the structure of Sculptor — together with those of Carina and Fornax — using  $V$ -band images taken with the MPG/ESO 2.2-m telescope at La Silla. The images have an areal coverage of 16.25 square degrees and reach a limiting magnitude of  $V \approx 23.5$ . The study derives major-axis core and limiting radii of  $7.56 \pm 0.7 \text{ arcmin}$  and  $40 \pm 4 \text{ arcmin}$ , respectively, using a King (1962) model, as did Irwin & Hatzidimitriou (1995). The  $1\text{-}\sigma$  disagreement between the two derived core radii is perhaps larger than expected from two data sets that have many stars in common. The apparently more serious disagreement between the two limiting radii is most likely due only to a larger true uncertainty in the limiting radius caused by uncertainties in the background surface density and the poor fit of the model to the outer part of the surface density profile. Walcher et al. (2003) confirms that the ellipticity of the surface-density contours increases with increasing projected radius; the contours also suggest “extensions” from the ends of the major axis that are interpreted as tidal tails. The radial projected density profile shows a “break” — a departure from the fitted King model — at around 30 arcmin, which the study interprets as evidence for the existence of an extended stellar component. Walcher et al. (2003) uses the relation between the King-model tidal radius, the mass, and the perigalacticon of a Galactic satellite developed by Oh, Lin, & Aarseth (1992) to deduce that Sculptor has a perigalacticon of 28 kpc.

A recent article by Coleman et al. (2005) does not confirm the finding in Walcher et al. (2003) that Sculptor has tidal tails and an extended stellar component. Instead, the analysis of photometric data in the  $V$  and  $I$  bands for a  $3.1^\circ \times 3.1^\circ$  field shows that a King model with a limiting radius of  $72.5 \pm 4.0 \text{ arcmin}$  is a satisfactory fit to the radial profile of stars that lie on the giant branch. The limiting magnitudes of the photometry are  $V = 20$  and  $I = 19$ , respectively. The study notes that oversubtracting the field population in its data produces a radial profile with the smaller fitted limiting radius and significant extratidal structure found in Walcher et al. (2003). Using additional information from the spectroscopy of 723 stars selected from the red giant branch, Coleman et al. (2005) derives an upper limit of  $2.3\% \pm 0.6\%$  for the contribution from stars beyond the tidal boundary to the total mass of Sculptor. The study does not find any conclusive evidence for tidal interaction between the Milky Way and Sculptor.

In contrast, Westfall et al. (2005) does find evidence. This study uses imaging in the  $M$ ,  $T_2$ , and  $DDO51$  bands to separate member giants from foreground dwarfs in a  $7.82 \text{ degrees}^2$  area that covers the eastward side of Sculptor including the central region. Candidate members are also selected from the region of the blue horizontal branch in the color-magnitude diagram. The selection of members is checked with spectroscopy for 147 candidates. The study finds members up to 150 arcmin from the center of Sculptor — the spatial extent of the survey and beyond the tidal boundary if that is identified with the measured King limiting radius of 80 arcmin. Several of these stars are spectroscopically-confirmed members. The radial surface brightness profile shows a break to a shallower slope at a radius of about 60 arcmin, which resembles the radial profiles seen in simulations of satellites interacting with the Milky Way (Johnston et al. 1999). Thus, Westfall et al. (2005) argues in favor of a significant tidal interaction between the Milky Way and Sculptor. It is beyond the scope of this work to resolve the apparent conflict between Coleman et al. (2005) and Westfall et al. (2005) by judging the merits of the analyses presented in both articles. Needless to say, a disagreement exists about the effect of the Galactic tidal field on the structure of Sculptor; measuring the

proper motion of the dSph may allow us to impose constraints on this effect.

Armandroff & Da Costa (1986) measured the radial velocities of 16 giants in Sculptor which average to produce a systemic heliocentric velocity of  $107.4 \pm 2.0 \text{ km s}^{-1}$ . This measurement alleviated the large uncertainty in this quantity, which existed due to mutually contradictory estimates from Hartwick & Sargent (1978) and Richter & Westerlund (1983). More recently, Queloz, Dubath, & Pasquini (1995) measured the radial velocities of 23 giant stars. The sample includes 15 stars observed previously by Armandroff & Da Costa (1986). The implied systemic heliocentric velocity of  $109.9 \pm 1.4 \text{ km s}^{-1}$  (after excluding two stars that are likely binaries) agrees within the quoted uncertainties with the measurement of Armandroff & Da Costa (1986). Our article adopts a mean velocity of  $109.9 \pm 1.4 \text{ km s}^{-1}$  for calculating the space velocity of Sculptor. Queloz, Dubath, & Pasquini (1995) finds no apparent rotation of the dSph around its minor axis. Tolstoy et al. (2004) measured radial velocities for 308 potential members of the dSph and find a systemic velocity of  $110 \text{ km s}^{-1}$ . There is no discussion of rotation, but Figure 4 in that article shows that the velocity dispersion does not increase with radius, as would be expected if there were a net rotation larger than the central dispersion. Interestingly, the study finds that the red horizontal branch stars have a more compact spatial distribution and a smaller velocity dispersion than the older and more metal-poor blue horizontal branch stars. The two most recent photometric and spectroscopic surveys by Coleman et al. (2005) and Westfall et al. (2005) confirm the greater central concentration of the more metal-rich stars. The two studies also find no evidence for rotation.

The mass-to-light ratio, ( $M/L$ ), of Sculptor is larger than a typical value for a Galactic globular cluster; it is, however, smaller than the  $M/L$ s for some other Galactic dSphs. Armandroff & Da Costa (1986) derives a central  $M/L_V$  of  $6.0 \pm 3.1$  and Queloz, Dubath, & Pasquini (1995) determines the somewhat larger value of  $13 \pm 6$ , in solar units. Both studies note that the measured  $M/L$  does not imply unequivocal support for dark matter in Sculptor.

The stars of Sculptor are old. Fitting isochrones to the principal sequences in the color-magnitude diagram, Da Costa (1984) finds that the majority of the stars are younger by “2–3 Gyr than Galactic globular clusters of similar metal abundance provided the helium abundances and the CNO/Fe ratios are also similar.” Da Costa (1984) also detects “blue stragglers” and estimates their age to be about 5 Gyr under the assumption that they are “normal” main-sequence stars, i.e., stars which did not acquire mass from a companion. No stars younger than 5 Gyr exist in Sculptor, indicating an absence of ongoing or recent star formation. However, Sculptor contains HI gas.

Carignan et al. (1998) and later Bouchard et al. (2003) detect two distinct clouds of HI that are diametrically opposite to each other almost along the minor axis and 20 – 30 arcmin from the center of the dSph. These clouds are within the tidal radius. The HI gas is very likely to be associated with Sculptor because its mean heliocentric velocity is similar to that of the dSph.

Carignan et al. (1998) discusses mechanisms that might account for the existence of the clouds. Removing the gas from the dSph by a time-dependent tidal force due the Milky Way is one possibility. Carignan et al. (1998) suggests that the alignment between the proper motion vector from Schweitzer et al. (1995) and a line passing through the two clouds supports this hypothesis for the origin of the clouds. However, if the tidal force affects the HI, it should also affect the stars and the possible signatures of tides in the stellar component of Sculptor are either absent or inconsistent with the direction of the Schweitzer et al. (1995) proper motion vector. For example, the increasing ellipticity of isodensity contours with increasing projected radius could be due to tides (e.g., Johnston, Spergel, & Hernquist 1995), but then the major axis should be along the proper motion vector. The possible “tidal extensions” reported by Walcher et al. (2003) are

at the ends of the major axis. If these extensions are a continuation of the increasing ellipticity, they also argue for an orbital plane parallel to the major axis. Walcher et al. (2003) claims that the eastern extension bends to the south, i.e., parallel to the minor axis and so argues that the orbital plane is aligned in the north-south direction. However, this alignment is inconsistent with the increasing ellipticity being due to the tidal force since, given the large distance of Sculptor, the Sun is nearly in the orbital plane and so the increasing ellipticity should be aligned with the tidal extensions.

Schweitzer et al. (1995) reports the first measurement of the proper motion for Sculptor:  $(\mu_\alpha, \mu_\delta) = (72 \pm 22, -6 \pm 25)$  mas century<sup>-1</sup>. This value includes contributions from the motions of the Sun and LSR; this article refers to this quantity as the “measured proper motion.” The measurement derives from 26 photographic plates imaged with a variety of ground-based telescopes using either a “blue”, B, or V filter. The earliest epoch is 1938 and the latest is 1991. The study estimates, among other quantities, the perigalacticon of the implied orbit. The best estimate ranges from 60 kpc for the “infinite halo” potential of the Milky Way to 78 kpc for the “point mass” potential. If the perigalacticon is no smaller than 60 kpc, then the Galactic tidal force has not played a significant role in the evolution of Sculptor. Numerical simulations of Piatek & Pryor (1995) or Oh, Lin, & Aarseth (1995) show that for a typical dSph, even with a  $M/L_V$  as low as 3, a perigalacticon of 60 kpc is too large for tides to have an important effect.

Motivated by the idea that some of the Galactic dSphs and globular clusters may be pieces of a tidally-disrupted progenitor satellite galaxy, several studies propose that they form “streams” in the Galactic halo. Lynden-Bell (1982) hypothesizes that Fornax, Leo I, Leo II, and Sculptor are members of the “FLS stream.” Majewski (1994) adds the newly-discovered Sextans to the FLS stream and recalculates its common plane — naming it the “FL<sup>2</sup>S<sup>2</sup> plane.” The FLS and the FL<sup>2</sup>S<sup>2</sup> planes differ only slightly. In a more extensive study, Lynden-Bell & Lynden-Bell (1995) infers that Sculptor may belong to one of three possible streams (see their Table 2). Stream # 2 contains the LMC, SMC, Draco, Ursa Minor, and, possibly, Sculptor and Carina; stream # 4a contains Sextans, Sculptor, Pal 3, and, possibly, Fornax; finally, stream # 4b contains Sextans, Sculptor, and, possibly, Fornax. For each stream, Lynden-Bell & Lynden-Bell (1995) calculates the expected proper motion of Sculptor.

Kroupa et al. (2004) notes that the 11 dwarf galaxies nearest to the Milky Way form a disk with a thickness to radius ratio of  $\leq 0.15$ . The article argues that the distribution expected for such nearby substructure in a cold-dark-matter universe is spherical, that the observed distribution is not, and, thus, that these objects are the tidal debris from the disruption of a larger satellite galaxy. In contrast, Kang et al. (2005) and Zentner et al. (2005) find that a planar distribution of nearby Galactic satellites is actually common in numerical simulations of galaxy formation. A direct comparison between the results of the simulations and the distribution of nearby satellites finds that they are consistent.

A test of the reality of streams or planar alignments is to measure the space motions of the satellites. Piatek et al. (2005; P05) reports a proper motion for Ursa Minor. The implied orbit for Ursa Minor is not in the plane defined by Kroupa et al. (2004). The proper motion also rules out membership in the stream proposed by Lynden-Bell & Lynden-Bell (1995). The measured proper motion for Carina (Piatek et al. 2003; P03) does not agree well with the predictions of Lynden-Bell & Lynden-Bell (1995), but is not precise enough to rule out membership in a stream. Piatek et al. (2002; P02) finds that a preliminary proper motion for Fornax is inconsistent with the predictions of Lynden-Bell & Lynden-Bell (1995) and that its direction is also inconsistent with an orbit in the FL<sup>2</sup>S<sup>2</sup> plane. Dinescu et al. (2004) reports an independent measurement of the proper motion of Fornax. This motion is consistent, within its uncertainty, with the predictions of Lynden-Bell & Lynden-Bell (1995) and the direction of this motion is along the great circle defined by the FL<sup>2</sup>S<sup>2</sup> plane. Dinescu et al. (2004) notes that the proper motion for Sculptor in Schweitzer et al. (1995) is

inconsistent with the  $FL^2S^2$  plane.

This article reports a second independent measurement of the proper motion for Sculptor and discusses the implications of the derived space motion on the dSph-Galaxy interaction. Section 2 describes observations and the data. The following section describes the analysis of the data leading to the derivation of the proper motion. Section 4.3 compares the proper motion from Schweitzer et al. (1995) with the one reported in this article. The next section, Section 5, integrates and describes the orbit of Sculptor. Section 6 discusses the implications of the orbit for the importance of the Galactic tidal force on the structure and internal kinematics of Sculptor, for the star formation history, and for the membership of Sculptor in the proposed streams of galaxies and globular clusters in the Galactic halo. The final section is a summary of the main results and conclusions.

## 2. Observations and Data

The Hubble Space Telescope (HST, hereafter) imaged two distinct fields in Sculptor using the Space Telescope Imaging Spectrograph (STIS, hereafter) in imaging mode with no filter (50CCD). Each field contains a known quasi-stellar object (QSO, hereafter), which serves as a reference point. The left panel of Figure 1 depicts the locations of the two fields on the sky: two small squares — one inside and the other outside of the core. The name of the field inside the core is SCL *J0100 – 3341*, which derives from the IAU designation of the QSO in this field. Tinney et al. (1997) confirms the identity of this QSO: it is at  $(\alpha, \delta) = (01^h00^m25^s.3, -33^\circ41'07'')$  (J2000.0), has a redshift  $z = 0.602 \pm 0.001$ , and has a magnitude  $B = 20.4$ . The observations of the SCL *J0100 – 3341* field occurred on September 24, 2000 and on September 26, 2002. At each epoch, there are three exposures at each of the eight dither pointings for the total of 24 images. The “ORIENTAT” angle — the position angle of the Y axis of the CCD measured eastward from north — is the same to within one-tenth of a degree for all of the exposures and equal to -67.5 degrees. The top-right panel in Figure 1 shows the SCL *J0100 – 3341* field. The QSO is in the cross-hair.

The name of the field outside of the core is SCL *J0100 – 3338*. The QSO in this field, also confirmed by Tinney et al. (1997), is at  $(\alpha, \delta) = (01^h00^m32^s.6, -33^\circ38'32'')$  (J2000.0), has a redshift  $z = 0.728 \pm 0.001$ , and has a magnitude  $B = 20.4$ . *HST* observed this field on September 13, 1999; September 28, 2000; and on September 28, 2002. At each of the three epochs, there are three exposures at each of the eight dither pointings for a total of 24 images. The “ORIENTAT” angle is the same to within one-tenth of a degree and equal to -69.3 degrees for all of the exposures for this field. The bottom-right panel of Figure 1 shows the SCL *J0100 – 3338* field. The QSO is in the cross-hair. Owing to its greater distance from the center of the dSph, the SCL *J0100 – 3338* field contains fewer stars than does the SCL *J0100 – 3341* field.

Bristow (2004) and P05 discuss the effect of the decreasing charge transfer efficiency of the STIS CCD on astrometric measurements. If not accounted for, the decreasing charge transfer efficiency may introduce a spurious contribution to a measured proper motion. Bristow & Alexov (2002) developed computer software which approximately restores an image taken with STIS to its pre-readout condition. All of the results that this article reports are based on images restored using the program of Bristow & Alexov (2002).

### 3. Analysis

P02 describes our method of deriving a proper motion from images taken with *HST* and containing at least one QSO. Fundamental to the method is the concept of an effective point-spread function (ePSF, hereafter), which Anderson & King (2000) describes in detail. The subsequent two articles in this series, P03 and P05, expand and improve upon the basic method. The analysis reported here incorporates only minor new features into the method; thus, the reader should consult those earlier articles for the details. Instead, this study mentions the major elements of the method alongside figures depicting key diagnostics of the performance of the method and briefly describes the new features.

#### 3.1. Flux Residuals

Equation 22 in P02 defines a “flux residual” diagnostic,  $\mathcal{RF}$ . It is the measure of how the shape of the constructed ePSF matches the shape of an image of an object. In the case of a perfect match,  $\mathcal{RF} = 0$ ; if the ePSF is narrower,  $\mathcal{RF} > 0$ ; otherwise,  $\mathcal{RF} < 0$ .

Several factors affect the shape of the PSF for an object. 1. Type of an object. A PSF for a galaxy is generally wider than that for a star, all else being equal. 2. Color of an object. Because of diffraction and aberrations, the width of the PSF is color-dependent. 3. Tilt or curvature of the focal plane. The PSF varies with location because the CCD surface and focal plane do not coincide everywhere. 4. Thermal expansion. Because the *HST* moves in and out of the Earth’s shadow, its temperature is continuously changing. These changes cause the telescope to expand or contract, affecting its focal length. 5. Charge traps in the CCD. As the packets of charge representing an object move along the  $Y$  axis (the direction of readout for STIS), those on its leading side fill partially each trap encountered, so that there are fewer traps available to remove charge from subsequent packets (Bristow & Alexov 2002). This non-uniform loss of charge across the object changes its PSF.

Given the aforementioned factors affecting the shape of the PSF, a plot of  $\mathcal{RF}$  versus the  $X$ - or  $Y$ -coordinate of an object will, in the best case, show that the points scatter around  $\mathcal{RF} = 0$ . In a less desirable case, the points may show trends with  $X$  or  $Y$  or both. These trends signal that the true PSF varies with location.

Because of the scarcity of stars in the observed fields, our method constructs a single and constant ePSF for a given field and epoch. A constant ePSF is one that does not vary with either  $X$  or  $Y$ . Figures 2 and 3 show plots of  $\mathcal{RF}$  versus  $X$  (panels in the left-hand column) and  $\mathcal{RF}$  versus  $Y$  (panels in the right-hand column) for the SCL *J0100 – 3341* and SCL *J0100 – 3338* fields, respectively. The rows of panels from top to bottom are each one epoch, arranged in chronological order. The filled squares in a plot correspond to the QSO. Note that the number of  $\mathcal{RF}$  values for a given object may be equal to the number of exposures — individual images — at a given epoch, or be less if the object is not measured in one or more exposures.

No panel in Figure 2, except for the top-left one, shows a trend between  $\mathcal{RF}$  and  $X$  or  $\mathcal{RF}$  and  $Y$ . The top-left panel shows that the mean  $\mathcal{RF}$  decreases linearly with  $X$ , implying that the shape of the true PSF becomes progressively narrower and more peaked than that of the constructed ePSF with increasing  $X$ . We are unable to trace the origin of this dependence. The values of  $\mathcal{RF}$  for the QSO are larger than those for other objects at both epochs and are all positive, implying that the true PSF for the QSO is wider than the constructed ePSF and than that for a star.

No panel in Figure 3 shows a trend as conspicuous as the one in the upper-left panel of Figure 2.

Nevertheless, the left-hand panel in the middle row does show a hint of variability of the true PSF with location. The PSF of the QSO in the SCL J0100 – 3338 is similar to that of a star. The values of  $\mathcal{RF}$ , though still biased towards positive values, are comparable to those for bright stars.

There are two reasons why the PSF of a QSO can be different from that of a star. 1. The underlying galaxy can broaden the image of a QSO. 2. The color of a typical QSO is bluer than that of a typical star. So, particularly for the unfiltered STIS imaging, the true PSF is narrower for a bluer object. Thus, depending on the interplay between the distance to a QSO and its color, the values of  $\mathcal{RF}$  for the QSO can average more positive than, more negative than, or the same as those for a bright star. Visual inspection of the QSO in the SCL J0100 – 3341 field shows what appears to be a single spiral arm or tidal feature extending from its image, suggesting that the underlying galaxy is indeed the cause of the large positive values of  $\mathcal{RF}$  for this QSO.

Experience with the data for other dSphs (P02, P03, and P05) has shown that trends in the  $\mathcal{RF}$  values with position do not necessarily produce systematic errors in the positions of objects. The next section searches for such systematic errors in the position.

### 3.2. Position Residuals

Fitting an ePSF to the science data array of an object (the  $5 \times 5$  array of pixels representing an object; see P02 for more detail on this array and our procedures) determines its centroid. With 24 images per field and epoch, there can be up to 24 measurements of the centroid. The actual number will be smaller than 24 if an object is flagged out from one or more images because its array is corrupted by cosmic rays or hot pixels. The dithering, rotation, and change of scale (e.g., due to “breathing” of the *HST*) between any two images cause the centroid of an object measured in these two images to differ. Therefore, at each epoch, every field has a fiducial coordinate system that coincides with the coordinate system of the first image in chronological order. The adopted transformation from the coordinate system of each subsequent image to the fiducial system contains a linear translation, rigid rotation, and a uniform scale change. Let  $(X_{0,j}^{i,k}, Y_{0,j}^{i,k})$  be the centroid of object  $i$  at epoch  $j$  in image  $k$  transformed to the fiducial coordinate system and the mean centroid of object  $i$  in the fiducial coordinate system of epoch  $j$  be  $(\langle X_{0,j} \rangle^i, \langle Y_{0,j} \rangle^i)$ . Define position residuals,  $\mathcal{RX}_j^{i,k}$  and  $\mathcal{RY}_j^{i,k}$ , for an object  $i$  as  $\mathcal{RX}_j^{i,k} = \langle X_{0,j} \rangle^i - X_{0,j}^{i,k}$  and  $\mathcal{RY}_j^{i,k} = \langle Y_{0,j} \rangle^i - Y_{0,j}^{i,k}$ . Ideally,  $\mathcal{RX}_j^{i,k} = \mathcal{RY}_j^{i,k} = 0$  for all  $j$  and  $k$ . Random noise causes  $\mathcal{RX}_j^{i,k}$  and  $\mathcal{RY}_j^{i,k}$  to differ from zero, but it does not cause any trends with respect to other quantities. However, systematic errors can cause such trends. Anderson & King (2000) demonstrates that a mismatch between the true PSF and the ePSF causes  $\mathcal{RX}_j^{i,k}$  and  $\mathcal{RY}_j^{i,k}$  to depend on the location of a centroid within a pixel — the pixel phase  $\Phi_x$  or  $\Phi_y$ . By definition,  $\Phi_{x,j}^{i,k} \equiv X_{0,j}^{i,k} - \text{Int}(X_{0,j}^{i,k})$  and  $\Phi_{y,j}^{i,k} \equiv Y_{0,j}^{i,k} - \text{Int}(Y_{0,j}^{i,k})$ , where the function  $\text{Int}(x)$  returns the integer part of the variable  $x$ .

Figure 4 plots  $\mathcal{RX}$  and  $\mathcal{RY}$  versus  $\Phi_x$  or  $\Phi_y$  for the SCL J0100 – 3341 field. The plots in the panel 4(a) are for the 2000 epoch and those in the panel 4(b) are for the 2002 epoch. The filled squares correspond to the QSO and the dots to stars with a  $S/N$  greater than 30.

The plots of  $\mathcal{RX}$  versus  $\Phi_x$  and  $\mathcal{RY}$  versus  $\Phi_y$  in Figures 4(a) and 4(b) show trends between these quantities for the QSO. Values of  $\mathcal{RX}$  and  $\mathcal{RY}$  tend to be negative for  $\Phi_x$  and  $\Phi_y$  less than about 0.5 pixel, and they tend to be positive for  $\Phi_x$  and  $\Phi_y$  greater than about 0.5 pixel. The points corresponding to the stars do not show these trends. The plots of the cross terms,  $\mathcal{RX}$  versus  $\Phi_y$  and  $\mathcal{RY}$  versus  $\Phi_x$ , do not show any trends for the QSO or for the stars. These trends indicate a mismatch between the ePSF and the true



PSF (Anderson & King 2000). Both stars with  $S/N > 15$  and the QSO contribute to the construction of the ePSF. Therefore, the more-extended true PSF of the QSO causes the ePSF to be wider than an ePSF constructed using only stars; in other words, the ePSF is a “compromise” between that of the stars and that of the QSO. An ePSF constructed using objects with  $S/N > 100$  diminishes the trends in the values of  $\mathcal{R}\mathcal{X}$  and  $\mathcal{R}\mathcal{Y}$  for the QSO because the shape of the ePSF is more akin to the shape of the true PSF of the QSO. However, increasing the  $S/N$  threshold to 100 or more in the construction of the ePSF is undesirable because the resulting ePSF is poorly sampled because there are only a few stars with  $S/N$  greater than this limit. Instead, we choose to allow the errors in the position of the QSO to remain and be reflected in a greater uncertainty for the measured proper motion for this field.

Figure 5 plots  $\mathcal{R}\mathcal{X}$  and  $\mathcal{R}\mathcal{Y}$  *versus*  $\Phi_x$  or  $\Phi_y$  for the SCL J0100 – 3338 field. Figures 5(a), 5(b), and 5(c) are for the 1999, 2000, and 2002 epochs, respectively. Only objects with a  $S/N$  greater than 15 are shown. No plot shows clear evidence for trends between  $\mathcal{R}\mathcal{X}$  or  $\mathcal{R}\mathcal{Y}$  and  $\Phi_x$  or  $\Phi_y$  for the QSO or for the stars. In this field, the true PSF of the QSO resembles that for a star, which is confirmed by Figure 3, where the values of  $\mathcal{R}\mathcal{F}$  for the QSO are indistinguishable from those for stars.

#### 4. Proper Motion of Sculptor

At this point, there are two lists of fiducial coordinates, one for each epoch, for the SCL J0100 – 3341 field, and three for the SCL J0100 – 3338 field. Define the standard coordinate system to be that which moves uniformly together with the stars of Sculptor. Thus, transforming the fiducial coordinates of a star of Sculptor from different epochs into the standard coordinate system produces the same value within the measurement uncertainties. In contrast, the transformed coordinates of the QSO or any other object that is not a member of Sculptor will show uniform motion. The proper motion of Sculptor derives from the motion of the QSO in the standard coordinate system.

P05 describes a procedure for deriving the motion of the QSO, and any other object that is not a member of the dSph, in the standard coordinate system from lists of fiducial coordinates at three epochs. The procedure includes a linear motion in the fitted transformations between the fiducial coordinate systems and the standard coordinate system for those objects whose  $\chi^2$  calculated with zero motion is above a threshold. The SCL J0100 – 3341 field has only two epochs, so we have modified the procedure for this case by excluding those objects with  $\chi^2$  values above a threshold from the calculation of the transformations between the coordinate systems. The motion of the QSO is just the difference of the two transformed coordinates. The following two sections describe the results from applying these procedures to the two fields.

##### 4.1. Motion of the QSO in the SCL J0100 – 3341 field

The number of objects with a measured centroid is 567 and 516 in epochs 2000 and 2002, respectively. Among these, 470 are common to the two epochs. The choice for the individual  $\chi^2$  that triggers fitting for uniform linear motion is 15. The multiplicative constant that ensures a  $\chi^2$  of one per degree of freedom is 1.151 (see P05 for a discussion of these parameters).

The transformation of the measured centroids to the standard coordinate system used in this article is

$$x_j'^i = x_{off} + c_1 + c_2(x_j^i - x_{off}) + c_3(y_j^i - y_{off}) \quad (1)$$

$$y_j'^i = y_{off} + c_4 + c_5(x_j^i - x_{off}) + c_6(y_j^i - y_{off}) \quad (2)$$

$$\sigma'_{xj}{}^i = \sqrt{(c_2\sigma_{xj}^i)^2 + (c_3\sigma_{yj}^i)^2} \quad (3)$$

$$\sigma'_{yj}{}^i = \sqrt{(c_5\sigma_{xj}^i)^2 + (c_6\sigma_{yj}^i)^2}. \quad (4)$$

The above represents a modification of the method described in P05, afforded here because of the greater number of stars. In the equations,  $c_1$  through  $c_6$  are the free parameters,  $(x_{off}, y_{off}) = (512, 512)$  pixel defines the reference point for the transformation, and  $(x_j^i, y_j^i)$  is a measured centroid of the  $i$ th object at the  $j$ th epoch which is transformed to  $(x_j^i, y_j^i)$  in the standard coordinate system.

Equations 10 and 11 in P05 define position residuals  $RX_{j-1}^i$  and  $RY_{j-1}^i$  for an object  $i$  transformed to the standard coordinate system from the fiducial coordinate system of the  $j$ th epoch. For an ideal case,  $RX_{j-1}^i = RY_{j-1}^i = 0$ . Figure 6 shows  $RX$  versus  $X$  and  $RY$  versus  $Y$  for the SCL J0100 – 3341 field. The most prominent feature is a “step” in  $RX_{1-1}$  versus  $X$  at  $X \simeq 320$  pixel. The values of  $RX_{1-1}$  tend to be negative for  $X$  below the step, indicating the presence of a systematic error in the  $X$  coordinates whose source we are unable to trace. The values of  $RX_{2-1}$  tend to be positive for  $X \lesssim 320$  pixel, which is forced by the fitting procedure.

An *ad hoc* approach for removing the “steps” is to replace  $x_j^i$  with  $x_j^i + c_7$  in the Equations 1 through 4 when  $x_j^i \leq 320$  pixels and to fit for the additional free parameter  $c_7$ . Applying this remedy removes the “steps,” as is shown by Figure 7 which plots the same quantities as Figure 6. In this corrected fitting procedure, the value of the multiplicative constant that ensures  $\chi^2$  of one per degree of freedom decreased to 1.123 because of the smaller residuals. The fitted value of  $c_7$  is 0.019 pixel. The proper motion for this field derives from this fit. Figure 8 is the same as Figure 7 except that the points are the weighted mean residuals in ten equal-length bins in  $X$  or  $Y$ . Note the different vertical scale. The points are plotted at the mean of the coordinate values in the bin. The average residuals show no systematic trends above a level of 0.001 pixel.

Figure 9 shows the location of the QSO as a function of time in the standard coordinate system. The top panel shows the variation of the  $X$  coordinate and the bottom panel does the same for the  $Y$  coordinate. The motion of the QSO is  $(\mu_x, \mu_y) = (0.0032 \pm 0.0032, 0.0005 \pm 0.0035)$  pixel yr<sup>−1</sup>. The contribution to the total  $\chi^2$  from the QSO, and from any other object whose motion was fit for, is 0 because a line always passes exactly through two points.

#### 4.2. Motion of the QSO in the SCL J0100 – 3338 field

The number of objects with measured centroids is 343, 326, and 314 in epochs 1999, 2000, and 2002, respectively. Among these, 257 are common to the three epochs. The choice for the individual  $\chi^2$  that triggers fitting for uniform linear motion is 15. The multiplicative constant that ensures a  $\chi^2$  of one per degree of freedom is 1.176.

Figures 10 and 11 show position residuals,  $RX$  and  $RY$ , as a function of position in the standard coordinate system for the SCL J0100 – 3338 field. They are analogous to Figures 6 and 8. From top to bottom, the rows of panels are for epochs 1999, 2000, and 2002. No panel shows unambiguous trends between  $RX$  and  $X$  or  $RY$  and  $Y$ . The largest deviations of the average residuals are  $RY \simeq 0.004$  pixel for  $Y < 100$  pixel. Any systematic trends at the location of the QSO are on the order of 0.001 pixel. Although not shown in the figures, the plots of the cross-terms do not show trends either.

Figure 12 is analogous to Figure 9 for the SCL J0100 – 3338 field. Note that the slopes in the corre-

sponding plots in Figures 12 and 9 need not be the same because the two fields are rotated with respect to each other — though for the fields in Sculptor the rotation is only a few degrees. The uncertainties shown for the points in Figure 12 are those calculated from the scatter of the measurements about the mean for an individual epoch increased by a multiplicative factor. The introduction of this factor reduces the contribution to the total  $\chi^2$  from the QSO. Without it, the contribution was 9.52. The contribution to the  $\chi^2$  has approximately two degrees of freedom, which implies a 0.9% probability of a  $\chi^2$  larger than 9.52 by chance. Such a small probability likely indicates the presence of unaccounted-for systematic errors. We choose to increase the uncertainty in our fitted proper motion by multiplying the uncertainties of the mean positions at each epoch by the same numerical factor so that contribution to the total  $\chi^2$  is about one per degree of freedom. Our fitting procedure calculates a value for the factor for all objects whose contribution to the total  $\chi^2$  exceeds 4.6, which is expected 10% of the time by chance. The value of the factor is 2.2 for the QSO and the uncertainty in the fitted motion of the QSO increases by essentially the same amount. The motion of the QSO is  $(\mu_x, \mu_y) = (-0.0043 \pm 0.0050, 0.0034 \pm 0.0038)$  pixel yr<sup>-1</sup>.

### 4.3. Measured Proper Motion

Table 1 gives the measured proper motion for each field in the equatorial coordinate system and their weighted mean. Table 2 tabulates the proper motions for those objects in the SCL J0100 – 3341 field for which it was measured. Table 3 does the same for the SCL J0100 – 3338 field. The first line of Table 2 and Table 3 corresponds to the QSO and subsequent objects are listed in order of decreasing  $S/N$ . The ID number of an object is in column 1, the  $X$  and  $Y$  coordinates of an object in the earliest image of the first epoch (o65q09010 for SCL J0100 – 3341 and o5bl02010 for SCL J0100 – 3338) are in columns 2 and 3, and the  $S/N$  of the object at the first epoch is in column 4. The components of the measured proper motion, expressed in the equatorial coordinate system, are in columns 5 and 6. Each value is the measured proper motion in the standard coordinate system corrected by adding the weighted mean proper motion of Sculptor given in the bottom line of Table 1. To indicate that this correction has been made, the proper motion of the QSO is given as zero. The listed uncertainty of each proper motion is the uncertainty of the measured proper motion, calculated in the same way as for the QSO, added in quadrature to that of the average proper motion of the dSph. The contribution of the object to the total  $\chi^2$  is in column 7. Although column 7 is in Table 2 for the sake of symmetry with Table 3, the  $\chi^2$  contributions are not meaningful.

Schweitzer et al. (1995) reports the first measurement of the proper motion for Sculptor; this study reports an additional two independent measurements. Figure 13 compares the three independent measurements, each represented by a rectangle. A dot at the center of a rectangle is the best estimate of the proper motion. The sides of a rectangle are offset from the center by the  $1\text{-}\sigma$  uncertainties. Rectangles 1, 2, and 3 represent the measurements by Schweitzer et al.(1995), this study (field SCL J0100 – 3341), and this study (field SCL J0100 – 3338), respectively.

The  $\alpha$  components of our measurements 2 and 3 agree almost exactly and their  $\delta$  components differ by only  $1.4\times$  the uncertainty of their difference. While the  $\delta$  component of measurement 1 agrees with the  $\delta$  components of measurements 2 and 3, the  $\alpha$  component does not agree with either one. The  $\alpha$  components of measurements 1 and 2 differ by  $2.3\times$  the uncertainty of their difference and those for measurements 1 and 3 differ by  $2.2\times$ . Because of the large difference in the  $\alpha$  components of the proper motion between the measurement from Schweitzer et al. (1995) and from our two fields, we choose to use the weighted average proper motion from Table 1 to determine the space velocity of Sculptor.

#### 4.4. Galactic Rest Frame Proper Motion

The measured proper motion of the dSph contains contributions from the motion of the LSR and the peculiar motion of the Sun. The magnitude of the contributions depend on the Galactic longitude and latitude of the dSph. Removing them yields the Galactic-rest-frame proper motion — the proper motion measured by a hypothetical observer at the location of the Sun but at rest with respect to the Galactic center. Columns (2) and (3) of Table 4 give the equatorial components,  $(\mu_\alpha^{\text{Grf}}, \mu_\delta^{\text{Grf}})$ , of the Galactic-rest-frame proper motion. Their derivation assumes:  $220 \text{ km s}^{-1}$  for the circular velocity of the LSR; 8.5 kpc for the distance of the Sun from the Galactic center; and  $(u_\odot, v_\odot, w_\odot) = (-10.00 \pm 0.36, 5.25 \pm 0.62, 7.17 \pm 0.38) \text{ km s}^{-1}$  (Dehnen & Binney 1998) for the peculiar velocity of the Sun, where the components are positive if  $u_\odot$  points radially away from the Galactic center,  $v_\odot$  is in the direction of rotation of the Galactic disk, and  $w_\odot$  points in the direction of the North Galactic Pole. Columns (4) and (5) give the Galactic-rest-frame proper motion in the Galactic coordinate system,  $(\mu_l^{\text{Grf}}, \mu_b^{\text{Grf}})$ . The next three columns give the  $\Pi$ ,  $\Theta$ , and  $Z$  components of the space velocity in a cylindrical coordinate system centered on the dSph. The components are positive if  $\Pi$  points radially away from the Galactic axis of rotation,  $\Theta$  points in the direction of rotation of the Galactic disk, and  $Z$  points in the direction of the North Galactic Pole. The derivation of these components assumes 87 kpc (Kaluzny et al. 1995) for the heliocentric distance to and  $109.9 \pm 1.4 \text{ km s}^{-1}$  (Queloz, Dubath, & Pasquini 1995) for the heliocentric radial velocity of Sculptor. The last two columns give the radial and tangential components of space velocity for an observer at rest at the Galactic center. The component  $V_r$  is positive if it points radially away from the Galactic center. Thus, at present, Sculptor is moving away from the Milky Way.

#### 5. Orbit and Orbital Elements of Sculptor

Knowing the space velocity of a dSph permits a determination of its orbit for a given form of the Galactic potential. This study adopts a Galactic potential that has a contribution from a disk of the form (Miyamoto & Nagai 1975)

$$\Psi_{\text{disk}} = -\frac{GM_{\text{disk}}}{\sqrt{R^2 + (a + \sqrt{Z^2 + b^2})^2}}, \quad (5)$$

from a spheroid of the form (Hernquist 1990)

$$\Psi_{\text{spher}} = -\frac{GM_{\text{spher}}}{R_{\text{GC}} + c}, \quad (6)$$

and from a halo of the form

$$\Psi_{\text{halo}} = v_{\text{halo}}^2 \ln(R_{\text{GC}}^2 + d^2). \quad (7)$$

In the above equations,  $R_{\text{GC}}$  is the Galactocentric distance,  $R$  is the projection of  $R_{\text{GC}}$  onto the plane of the Galactic disk, and  $Z$  is the distance from the plane of the disk. All other quantities in the equations are adjustable parameters and their values are the same as those adopted by Johnston, Sigurdsson, & Hernquist (1999):  $M_{\text{disk}} = 1.0 \times 10^{11} M_\odot$ ,  $M_{\text{spher}} = 3.4 \times 10^{10} M_\odot$ ,  $v_{\text{halo}} = 128 \text{ km s}^{-1}$ ,  $a = 6.5 \text{ kpc}$ ,  $b = 0.26 \text{ kpc}$ ,  $c = 0.7 \text{ kpc}$ , and  $d = 12.0 \text{ kpc}$ .

Figure 14 shows the projections of the orbit of Sculptor onto the  $X-Y$  (top-left panel),  $X-Z$  (bottom-left panel), and  $Y-Z$  (bottom-right panel) Cartesian planes. The orbit results from an integration of the motion in the Galactic potential given by Equations 5, 6, and 7. The integration extends for 3 Gyr backwards in time and begins at the current location of Sculptor with the negative of the space velocity components

given in the bottom line of columns (6), (7), and (8) of Table 4. The filled square marks the current location of the dSph, the filled star indicates the center of the Galaxy, and the two small circles mark the points on the orbit where  $Z = 0$  or, in other words, where the orbit crosses the plane of the Galactic disk. The large circle is for reference: it has a radius of 30 kpc. In the right-handed coordinate system of Figure 14, the current location of the Sun is on the positive  $X$ -axis. The figure shows that Sculptor is moving away from the Milky Way, is closer to perigalacticon than apogalacticon, and that it has a nearly polar orbit with a modest eccentricity.

Table 5 tabulates the elements of the orbit of Sculptor. The value of the quantity is in column (4) and its 95% confidence interval is in column (5). The latter comes from 1000 Monte Carlo experiments, where an experiment integrates the orbit using an initial velocity that is generated by randomly choosing the line-of-sight velocity and the two components of the measured proper motion from Gaussian distributions whose mean and standard deviation are the best estimate of the quantity and its quoted uncertainty, respectively. The eccentricity of the orbit is defined as

$$e = \frac{(R_a - R_p)}{(R_a + R_p)}. \quad (8)$$

The most likely orbit has about a 2:1 ratio of apogalacticon to perigalacticon, though the 95% confidence interval for the eccentricity allows ratios approximately between 1.7:1 and 4:1. The orbital period of Sculptor, 2.2 Gyr, is about 50% longer than those of Carina (1.4 Gyr; P03) and Ursa Minor (1.5 Gyr; P05).

## 6. Discussion

Knowing the orbit can help answer several questions about Sculptor, or, at least, increase the level of our understanding of this galaxy. These questions are: 1. Is Sculptor a member of a stream of galaxies? 2. Is its star formation history correlated with the orbit? 3. What is the origin of the HI clouds detected in close proximity to the dSph? 4. Does Sculptor contain dark matter?

### 6.1. Is Sculptor a Member of a Stream?

Lynden-Bell & Lynden-Bell (1995) proposes that Sculptor may be a member of one of three possible streams: stream No. 2 (together with the LMC, SMC, Draco, Ursa Minor, and Carina); No. 4a (together with Sextans, Pal 3, and Fornax); or No. 4b (together with Sextans and Fornax). Columns (2) and (3) in Table 6 give the predicted heliocentric (i.e., “measured” in our terminology) proper motion in the equatorial coordinate system for Sculptor if it indeed belongs to any of the three streams. The magnitude of the proper motion vector,  $|\vec{\mu}| = \sqrt{\mu_\alpha^2 + \mu_\delta^2}$ , and its position angle are in columns (4) and (5). For easy comparison, the corresponding quantities from our study are in the bottom line of the table. Comparing the entries shows that the predictions for streams 2 and 4a disagree significantly with our measurement. However, the prediction for stream No. 4b is closer: the magnitudes differ by  $1.6\times$  the uncertainty in their difference, while the position angles differ by  $1.6\times$ . Differences of this size should occur by chance 1% of the time. The measured proper motion based on only the three-epoch data in the SCL  $J0100 - 3338$  field improves the agreement with the prediction for stream 4b. Thus, while we rule out the possibility that Sculptor is a member of stream No. 2 or 4a, its membership in stream 4b is possible.

Stream 4b contains both Sculptor and Fornax. The Dinescu et al. (2004) proper motion for Fornax is  $(\mu_\alpha, \mu_\delta) = (59 \pm 16, -15 \pm 16)$  mas cent<sup>-1</sup>. The magnitude and position angle of the proper motion are

$61 \pm 16 \text{ mas cent}^{-1}$  and  $104 \pm 15$  degrees. The prediction for stream 4b from Lynden-Bell & Lynden-Bell (1995) is  $20 \text{ mas cent}^{-1}$  and 162 degrees. The difference between the measured and predicted proper motions would be this large or larger by chance only 0.4% of the time. Thus, the physical reality of stream 4b is doubtful.

Dinescu et al. (2004) argues that Fornax and Sculptor are members of the same stream that also includes Leo I, Leo II, and Sextans. Together the galaxies define the FL<sup>2</sup>S<sup>2</sup> plane. If they do form a stream, their Galactic-rest-frame proper motion vectors should be aligned with the great circle passing through the galaxies. The position angle of the great circle passing through Sculptor and Fornax is about 99 degrees at the location of Sculptor and 95 degrees at Fornax. The position angle of the Galactic-rest-frame proper motion for Fornax reported by Dinescu et al. (2004) is  $79 \pm 25$  degrees, which differs by  $0.64\times$  its uncertainty from the position angle of the great circle. If Sculptor and Fornax form a stream, then they should move in the same direction along the great circle connecting them. Thus, the proper motion of Fornax from Dinescu et al. (2000) implies that the position angle of the Galactic-rest-frame proper motion of Sculptor should be 99 degrees. The position angle for the proper motion of Sculptor reported here is  $333 \pm 15$  degrees, which differs from the prediction by  $8.4\times$  its uncertainty. Discounting the proper motion from this study and instead using the position angle of  $40 \pm 24$  degrees implied by the proper motion measured by Schweitzer et al. (1995) does not remove the disagreement: the position angle differs by  $2.5\times$  its uncertainty from that of the great circle. We conclude that Sculptor and Fornax do not belong to the same stream.

Kroupa et al. (2004) shows that the 11 dwarf galaxies nearest to the Milky Way are nearly on a plane, whose two poles are at  $(\ell, b) = (168, -16)$  degrees and  $(348, +16)$  degrees. Adopting the direction of the angular momentum vector as the pole of the orbit, then the location of the pole is

$$(\ell, b) = (\Omega + 90^\circ, \Phi - 90^\circ). \quad (9)$$

Because of the left-handed nature of the Galactic rotation, prograde orbits have  $b < 0$  and retrograde orbits have  $b > 0$ . Thus, the pole of our orbit for Sculptor is  $(\ell, b) = (5 \pm 16, -4 \pm 1.6)$  degrees, where the uncertainties are  $1\text{-}\sigma$  values from the Monte Carlo simulations. The galactic longitudes of the poles of the plane and orbit agree within the uncertainty, but the galactic latitudes do not. They differ by 20 degrees, which is more than  $12\times$  the uncertainty in the location of the pole of the orbit. However, there is also some uncertainty in the orientation of the plane passing through the dwarf galaxies near the Milky Way. We conclude the plane of the orbit of Sculptor is similar to the plane defined by the nearby dwarf galaxies.

## 6.2. The Effect of the Galactic Tidal Force on the Structure of Sculptor

The measured ellipticity of the isodensity contours increases with projected distance from the center of Sculptor (see Figure 1 in Irwin & Hatzidimitriou 1995), akin to surface density contours of a model dSph in the numerical simulations of Johnston, Spergel, & Hernquist (1995; e.g., see Figure 4). If the Galactic tidal force deformed Sculptor from an initial nearly-spherical shape to its present elongated shape in the outer regions then, from our vantage point nearly in the orbit plane, the position angle of its projected major axis should be similar to — or differ by 180 degrees from — the position angle of the Galactic-rest-frame proper motion vector, as predicted by the numerical simulations of Oh, Lin, & Aarseth (1995), Piatek & Pryor (1995), or Johnston, Spergel, & Hernquist (1995). The position angle of the projected major axis is  $99 \pm 1$  degrees and the position angle of our measured Galactic-rest-frame proper motion vector is  $333 \pm 15$  degrees. Allowing for the 180-degree degeneracy, the difference between the two position angles is  $3.6\times$  the uncertainty of their difference, which suggests that the Galactic tidal force has not elongated

Sculptor.

### 6.3. Does Star Formation History Correlate with the Orbital Motion of Sculptor?

Da Costa (1984) imaged a  $3 \text{ arcmin} \times 5 \text{ arcmin}$  field located just outside of the core radius of Sculptor in three bands:  $B$ ,  $V$ , and  $R$ . The photometry reaches the main-sequence turn off. Comparing theoretical isochrones with the distribution of stars in the color-magnitude diagram, the study finds that the majority of stars is about 2-3 Gyr younger than the galactic globular clusters of comparable metal abundance. An earlier study by Kunkel & Demers (1977) based on  $B$  and  $V$  photometry extending to 0.4 magnitudes below the horizontal branch reaches a similar conclusion. The color-magnitude diagram also shows a population of “blue stragglers,” which might be indicative of an extended period of star formation. Da Costa (1984) concludes, however, that, if an intermediate-age stellar population exists in Sculptor, it is “infinitesimal compared to that of the Carina system.”

Deep *HST* imaging by Monikiewicz et al. (1999) in a single field, reaching 3 magnitudes below the main-sequence turn-off, confirms the basic picture of Sculptor uncovered by Kunkel & Demers and Da Costa (1984). This color-magnitude diagram also reveals the presence of “blue stragglers” and implies an age comparable to that of the galactic globular clusters. The small number of stars in the small field made a search for an intermediate-age stellar population inconclusive.

Majewski et al. (1999), Hurley-Keller et al. (1999), and Harbeck et al. (2001) use wide-field imaging to show the presence of two stellar populations with distinctly different metallicities ( $[\text{Fe}/\text{H}] = -2.3$  and  $-1.5$ ; Majewski et al. 1999). The more metal rich population is more centrally concentrated in the galaxy. Most recently, Tolstoy et al. (2004) confirms the above picture using wide-field imaging and spectroscopy. Spectroscopically-determined metallicities range from  $-2.8$  to  $-0.9$ . Stars more metal-rich than  $-1.7$  are more centrally concentrated and have a smaller velocity dispersion than the rest of the sample. However, both stellar populations are older than 10 Gyrs.

The aforementioned studies show that there were at least two episodes of star formation at times more than 10 Gyr ago. Because 10 Gyrs is much longer than the orbital period of approximately 2.2 Gyr, there is no clear connection between the stimulation of star formation and processes such as the Galaxy-Sculptor tidal interaction or the effects of ram pressure. The lack of correlation could be due to the loss of all of the gas in Sculptor about 10 Gyr ago. But, surprisingly, the observations indicate that Sculptor has HI today.

### 6.4. HI Gas in Sculptor

Unlike most other Galactic dSphs, Sculptor contains a detectable amount of HI. Knapp et al. (1978) detects three clouds of HI in the vicinity of Sculptor and speculates that one of them, with a radial velocity of  $120 \text{ km s}^{-1}$ , may be associated with Sculptor, whose radial velocity at the time was uncertain. Carignan et al. (1998) confirms and refines this detection and puts a lower limit on the mass of HI of  $3.0 \times 10^4 M_{\odot}$ . Bouchard et al. (2003) repeats the observations over a wider field with the Parkes single-dish telescope and, over a smaller region, at higher angular resolution with the Australia Telescope Compact Array. The better data show that the HI is not associated with a background galaxy and the probability of a chance superposition of a galactic high velocity cloud is less than 2%. These arguments, together with the agreement within  $4 \text{ km s}^{-1}$  of the radial velocity of the HI and the radial velocity of Sculptor make a strong case for

the physical association of the clouds with the dSph.

The gas is in two clouds. Figure 15 shows the distribution of HI on the sky in the direction of Sculptor based on the Australia Telescope Compact Array data from Bouchard et al. (2003). The asterisk marks the optical center of Sculptor and the two clouds are about 20–30 arcmin from the center, one to the northeast and one to the southwest. The masses of the clouds are  $(4.1 \pm 0.2) \times 10^4 M_\odot$  and  $(1.93 \pm 0.02) \times 10^5 M_\odot$ , respectively. The two clouds lie nearly along the minor axis of the dSph; the orientation of Sculptor is shown in Figure 15 by the ellipse representing the optical boundary.

Although the association between the gas and the dSph seems well-established, why Sculptor still has gas when most of the other galactic dSphs do not and the cause of the observed configuration of the gas are debated. Mayer et al. (2005) studies the loss of gas from dwarf galaxies in the Local Group using numerical simulations that include ram pressure stripping. It quantifies the expected result that a galaxy with a deeper potential well or with a larger perigalacticon is more likely to retain its gas. The orbit of Sculptor is similar to those of Carina and Ursa Minor, which suggests that differences in the degree of tidal shocking or ram pressure stripping are not the reason for the difference in gas retention. However, note that the 95% confidence intervals for the perigalacticons of all three orbits are still too large to make a conclusive statement. The larger mass of Sculptor compared to Carina and Ursa Minor is the most likely reason why it was able to retain gas.

Mechanisms that could affect the distribution of HI within the dSph are tidal interaction, ram pressure, and forces from supernovae or winds from young stars. Tidal interaction and ram pressure tend to spread the gas in the plane of the orbit. The two arrows in Figure 15 represent the Galactic-rest-frame proper motions as measured by Schweitzer et al. (1995; dashed) and this study (solid). The ratio of their lengths is the same as the ratio of the magnitudes of the proper motions. The dotted line is a section of a great circle that passes through Sculptor and Fornax; its position angle is 99 degrees.

The Schweitzer et al. (1995) proper motion (dashed arrow) is nearly aligned with the line that connects the centers of the clouds. Carignan et al. (1998) notes this alignment and suggests that it may indicate a “tidal” origin for the clouds: presumably, the Galactic tidal force stretches the gas, initially centered within the dSph, into its observed distribution. The most serious problem with such a picture is that the tidal force would stretch the distribution of both the stars and the gas, which then aligns the major axes of the gaseous and stellar distributions from our perspective as an observer nearly in the plane of the orbit of Sculptor. They are not aligned, perhaps because the motion of the gas is governed by both gravitational forces and pressure gradients. As was noted in Section 6.2, if the observed ellipticity of Sculptor is due to the tidal force, then the Galactic-rest-frame proper motion should be aligned with the major axis. Figure 15 shows that the solid arrow, our measurement, is closer to such an alignment than the dashed arrow. Because the tidal force is zero at the center of a dSph, it cannot by itself separate a single cloud centered on the dSph into two clouds. Thus, within the context of a picture in which tides have had an important effect on Sculptor, our proper motion is more plausible than that of Schweitzer et al. (1995). However, is our proper motion consistent with the geometry of the two clouds?

We think yes. First, the two clouds are elongated in the direction of our proper motion (see particularly Figure 1 in Bouchard et al. 2003). The observed elongation could be due to ram pressure from the motion through a gaseous Galactic halo. Second and more speculatively, the two clouds could be due to the Rayleigh-Taylor instability when the HI in Sculptor moves through the hot and low-density gaseous halo. Or the gas could have been squeezed out perpendicular to the direction of motion by the compressive tidal shock when Sculptor crosses the Galactic disk. Expansion combined with infall of the gas forms a ring that looks like



two clouds in projection.

### 6.5. Is there dark matter in Sculptor?

Estimates of the  $M/L_V$  for Sculptor range from 6 – 13 and estimates of the limiting radius range from about 40 – 80 arcmin. The estimates of  $M/L$  assume that mass follows light. If this is true, then the implied mass of Sculptor must be large enough, given our orbit, to produce a tidal radius that is at least as large as the observed limiting radius. Equating the tidal radius and the limiting radius predicts a value for  $M/L$ , which should agree with the measured value. Also, the dSph must have a mass and, hence,  $M/L$  large enough for it to have survived destruction by the Galactic tidal force on our orbit.

In lieu of numerical simulations, an approximate analytical approach is to calculate the tidal radius,  $r_t$ , beyond which a star becomes unbound from the dSph. For a logarithmic Galactic potential,  $r_t$  is given by (King 1962; Oh, Lin, & Aarseth 1992)

$$r_t = \left( \frac{(1-e)^2}{[(1+e)^2/2e] \ln[(1+e)/(1-e)] + 1} \frac{M}{M_G} \right)^{1/3} a. \quad (10)$$

Here  $e$  is eccentricity of the orbit,  $a$  is the semi-major axis ( $a \equiv (R_a + R_p)/2$ ),  $M$  is the mass of the dSph, and  $M_G$  is the mass of the Galaxy within  $a$ . Equating  $r_t$  with the observed limiting radius derived by fitting a King (1966) model,  $r_k$ , gives a value for  $M/L_V$  for a given orbit. If  $r_k = 40$  arcmin, then 28% of the orbits in Monte Carlo simulations have  $M/L_V > 6$  and 10% of the orbits have  $M/L_V > 13$ . If  $r_k = 80$  arcmin, then 100% of the orbits have  $M/L_V > 13$ . These results show that the global  $M/L$  of Sculptor is probably larger than the measured  $M/L$ , if the larger of the measured limiting radii is identified with the tidal radius. The  $M/L$  calculated assuming that mass follows light underestimates the true global  $M/L$  if Sculptor contains dark matter that is more spatially extended than the luminous matter (e.g., Pryor & Kormendy 1990). However, equation 10 shows that  $M \propto r_t^3$ , so the values for  $M/L$  derived using this equation are sensitive to the measured value of the limiting radius. Until kinematic measurements definitively identify the tidal radius, an  $M/L$  derived with the above argument should be treated with caution.

The average of the measured values of  $M/L_V$  for Galactic globular clusters is 2.3 (Pryor & Meylan 1993). Could the true  $M/L_V$  of Sculptor be similar to this average? Numerical simulations by Oh, Lin, & Aarseth (1995) and Piatek & Pryor (1995) show that the ratio of the limiting radius derived by fitting a theoretical King model (King 1966),  $r_k$ , to the tidal radius defined by Equation (10) is a useful indicator of the importance of the Galactic tidal force on the structure of a dSph. These simulations show that: if  $r_k/r_t \lesssim 1.0$ , the Galactic tidal force has little effect on the structure of the dSph; at  $r_k/r_t \approx 2.0$ , the effect of the force increases rapidly with increasing  $r_k/r_t$ ; and, for  $r_k/r_t \approx 3.0$ , the dSph disintegrates in a few orbits. Assuming that  $M/L_V = 2.3$  and  $r_k = 40$  arcmin,  $r_k/r_t > 2.0$  for 6% of the orbits generated in Monte Carlo simulations. If  $r_k = 80$  arcmin, the fraction is 100%. Thus, it is possible that Sculptor could have survived for a Hubble time on its current orbit if it only contains luminous matter. We conclude that measured orbit of Sculptor does not require it to contain dark matter.

### 6.6. A Lower Limit for the Mass of the Milky Way

Sculptor is bound gravitationally to the Milky Way. The Galactocentric space velocity of the dSph imposes a lower limit on the mass of the Milky Way within the present Galactocentric radius of the dSph,

$R$ . Assuming a spherically symmetric mass distribution and zero for the total energy of the dSph, the lower limit for the mass of the Milky Way is given by

$$M = \frac{R (V_r^2 + V_t^2)}{2G}. \quad (11)$$

Setting  $R = 87$  kpc and using the values from Table 4 for  $V_r$  and  $V_t$ ,  $M = (4.6 \pm 2.0) \times 10^{11} M_\odot$ . This lower limit is consistent with other recent estimates of the mass of the Milky Way, such as the mass of  $5.4_{-0.4}^{+0.1} \times 10^{11} M_\odot$  within  $R = 50$  kpc found by Sakamoto, Chiba, & Beers (2003). The Milky Way potential adopted in Section 5 has a mass of  $7.8 \times 10^{11} M_\odot$  out to  $R = 87$  kpc.

## 7. Summary

This article presents a measurement of the proper motion of Sculptor using data taken with *HST* and STIS in imaging mode. Using this measurement, it derives the orbit and discusses: membership in proposed streams, tidal interaction with the Milky Way, the relation between the orbit and the star-formation history, the HI gas associated with the dSph, the dark matter content, and a lower limit on the mass of the Milky Way. The list below enumerates our findings.

1. Two independent measurements of the proper motion give a weighted mean value of  $(\mu_\alpha, \mu_\delta) = (9 \pm 13, 2 \pm 13)$  mas cent<sup>-1</sup> in the equatorial coordinate system for a heliocentric observer.
2. Removing the contributions to the measured proper motion from the motions of the Sun and of the LSR gives a Galactic-rest-frame proper motion of  $(\mu_\alpha^{\text{Grf}}, \mu_\delta^{\text{Grf}}) = (-23 \pm 13, 45 \pm 13)$  mas cent<sup>-1</sup> in the equatorial coordinate system for an observer at the location of the Sun but at rest with respect to the Galactic center. In the Galactic coordinate system this motion is  $(\mu_l^{\text{Grf}}, \mu_b^{\text{Grf}}) = (11 \pm 13, -50 \pm 14)$  mas cent<sup>-1</sup>.
3. The radial and tangential components of the space velocity are  $V_r = 79 \pm 6$  km s<sup>-1</sup> and  $V_t = 198 \pm 50$  km s<sup>-1</sup>, respectively, as measured by a Galactocentric observer at rest.
4. The best estimate of the orbit shows that Sculptor is approaching its apogalacticon of  $R_a = 122$  kpc on a polar orbit with eccentricity  $e = 0.29$ . The perigalacticon of the orbit is  $R_p = 68$  kpc and the orbital period is  $T = 2.2$  Gyr.
5. Sculptor is not a member of streams 2 and 4a proposed by Lynden-Bell & Lynden-Bell (1995). It could be a member of stream 4b, though the proper motion of Fornax measured by Dinescu et al. (2004) makes the physical reality of this stream doubtful.
6. The proper motion vectors of Sculptor and Fornax show that they cannot be members of the same stream.
7. The pole of the orbit of Sculptor is 26 degrees from the pole of the plane of the Galactic dSphs noted by Kroupa et al. (2004). This difference is much larger than the uncertainty in the pole of the orbit, but is probably within the uncertainty of the definition of the plane of the dSphs.
8. A comparison of the orbit of Sculptor to those of other dSphs does not provide a clear reason for why Sculptor contains HI while the others do not. The origin and distribution of HI remain puzzling. This article proposes that, while the line connecting the two clouds of HI is nearly perpendicular to our Galactic-rest-frame proper motion, some combination of ram pressure, tidal interaction, and Rayleigh-Taylor instability could produce this geometry.

We thank the anonymous referee for comments that helped to improve the presentation of our work. We also thank Sergei Maschenko for pointing out to us that our method for propagating uncertainties from the measured proper motions to the space velocity was incorrect. CP and SP acknowledge the financial support of the Space Telescope Science Institute through the grants HST-GO-07341.03-A and HST-GO-08286.03-A and from the National Science Foundation through the grant AST-0098650. EWO acknowledges support from the Space Telescope Science Institute through the grants HST-GO-07341.01-A and HST-GO-08286.01-A and from the National Science Foundation through the grants AST-9619524 and AST-0098518. MM acknowledges support from the Space Telescope Science Institute through the grants HST-GO-07341.02-A and HST-GO-08286.02-A and from the National Science Foundation through the grant AST-0098661. DM is supported by FONDAF Center for Astrophysics 15010003.

## REFERENCES

- Anderson, J., & King, I. R. 2000, *PASP*, 112, 1360
- Armandroff, T. E., & Da Costa, G. S. 1986, *AJ*, 92, 777
- Baade, W., & Hubble, E. P. 1939, *PASP*, 51, 40
- Bouchard, A., Carignan, C., & Mashchenko, S. 2003, *AJ*, 126, 1295
- Bristow, P. 2004, CE-STIS-2004-003
- Bristow, P. & Alexov, A. 2002, CE-STIS-ISR 2002-001
- Carignan, C., Beaulieu, S., Cote, S., Demers, S., & Mateo, M. 1998, *AJ*, 116, 1690
- Coleman, M. G., Da Costa, G. S., & Bland-Hawthorn, J. B. 2005, 130, 1065
- Da Costa, G. S. 1984, *ApJ*, 285, 483
- Dehnen, W., & Binney, J. J. 1998, *MNRAS*, 298, 387
- Demers, S., Kunkel, W. E., & Krautter, A. 1980, *AJ*, 85, 1587
- Dinescu, D. I., Keeney, B. A., Majewski, S. R., & Girard, T. M. 2004, *AJ*, 128, 687
- Eskridge, P. B. 1988a, *AJ*, 95, 1706
- Eskridge, P. B. 1988b, *AJ*, 96, 1336
- Harbeck, D. et al. 2001, *AJ*, 122, 3092
- Hartwick, F. D. A., & Sargent, W. L. W. 1978, *ApJ*, 221, 512
- Hernquist, L. 1990, *ApJ*, 356, 359
- Hodge, P. 1965, *ApJ*, 142, 1390
- Hurley-Keller, D., Mateo, M., & Grebel, E. K. 1999, 523, L25
- Irwin, M. J., & Hatzidimitriou, D. 1995, *MNRAS*, 277, 1354
- Johnston, K. V., Sigurdsson, S., & Hernquist, L. 1999, *MNRAS*, 302, 771
- Johnston, K. V., Spergel, D. N., & Hernquist, L. 1995, *ApJ*, 451, 598
- Kaluzny, J., Kubiak, M., Szymański, M., Udalski, A., Krzemiński, W., & Mateo, M. 1995, *A&ASS*, 112, 407
- Kang, X., Mao, S., Gao, L., Jing, Y. P. 2005, *A&A*, in press (astro-ph/0501333)
- King, I. 1962, *AJ*, 67, 471
- King, I. 1966, *AJ*, 71, 64
- Knapp, G. R., Kerr, F. J., & Bowers, P. F. 1978, *AJ*, 83, 360
- Kroupa, P., Theis, C., & Boily, C. M. 2004, *A&A*, in press
- Kunkel, W. E., & Demers, S. 1977, *ApJ*, 214, 21
- Lynden-Bell, D. 1982, *Observatory*, 102, 202
- Lynden-Bell, D., & Lynden-Bell, R. M. 1995, *MNRAS*, 275, 429
- Majewski, S. R. 1994, *ApJ*, 431, L17
- Majewski, S. R., Siegel, M. H., Patterson, R. J., & Rood, R. T. 1999, *ApJ*, 520, L33
- Mateo, M. 1998, *ARAA*, 36, 435

- Mayer, L., Mastropietro, C., Wadsley, J., Stadel, J., & Moore, B. 2005, MNRAS, submitted (astro-ph/0504277)
- Miyamoto, M., & Nagai R. 1975, PASJ, 27, 533
- Monkiewicz, J. et al. 1999, PASP, 111, 1392
- Oh, K. S., Lin, D. N. C., & Aarseth, S. J. 1992, ApJ, 386, 506
- Oh, K. S., Lin, D. N. C., & Aarseth, S. J. 1995, ApJ, 442, 142
- Piatek, S., & Pryor, C. 1995, AJ, 109, 1071
- Piatek, S., Pryor, C., Olszewski, E. W., Harris, H. C., Mateo, M., Minniti, D., Monet, D. G., Morrison, H., & Tinney, C. G. 2002, AJ, 124, 3198 (P02)
- Piatek, S., Pryor, C., Olszewski, E. W., Harris, H. C., Mateo, M., Minniti, D., & Tinney, C. G. 2003, AJ, 126, 2346 (P03)
- Piatek, S., Pryor, C., Bristow, P., Olszewski, E. W., Harris, H. C., Mateo, M., Minniti, D., & Tinney, C. G. 2005, AJ, in press (P05)
- Pryor, C., & Kormendy, J. 1990, AJ, 100, 127
- Pryor, C., & Meylan, G. 1993, in Structure and Dynamics of Globular Clusters, edited by S. Djorgovski & G. Meylan (ASP, San Francisco), p. 357
- Queloz, D., Dubath, P., & Pasquini, L. 1995, A&A, 300, 31
- Richter, H. B., & Westerlund, B. E. 1983, ApJ, 264, 114
- Sakamoto, T., Chiba, M., & Beers, T. C. 2003, A&A, 397, 899
- Schweitzer, A. E., Cudworth, K. M., Majewski, S. R., & Suntzeff, N. B. 1995, AJ, 110, 2747
- Shapley, H. 1938, Harv. Obs. Bull., 908, 1
- Tinney, C. G., Da Costa, G. S., & Zinnecker, H. 1997, MNRAS, 285, 111
- Tolstoy, E., et al. 2004, ApJ, 617, L119
- Walcher, C. J., Fried, J. W., Burkert, A., & Klessen, R. S. 2003, A&A, 406, 847
- Westfall, K. B., Majewski, S. R., Ostheimer, J. C., Frinchaboy, P. M., Kunkel, W. E., Patterson, R. J., & Link, A. 2005, astro-ph/0508091
- Zentner, A. R., Kravtsov, A. V., Gnedin, O. Y., Klypin, A. A. 2005, ApJ, in press (astro-ph/0502496)

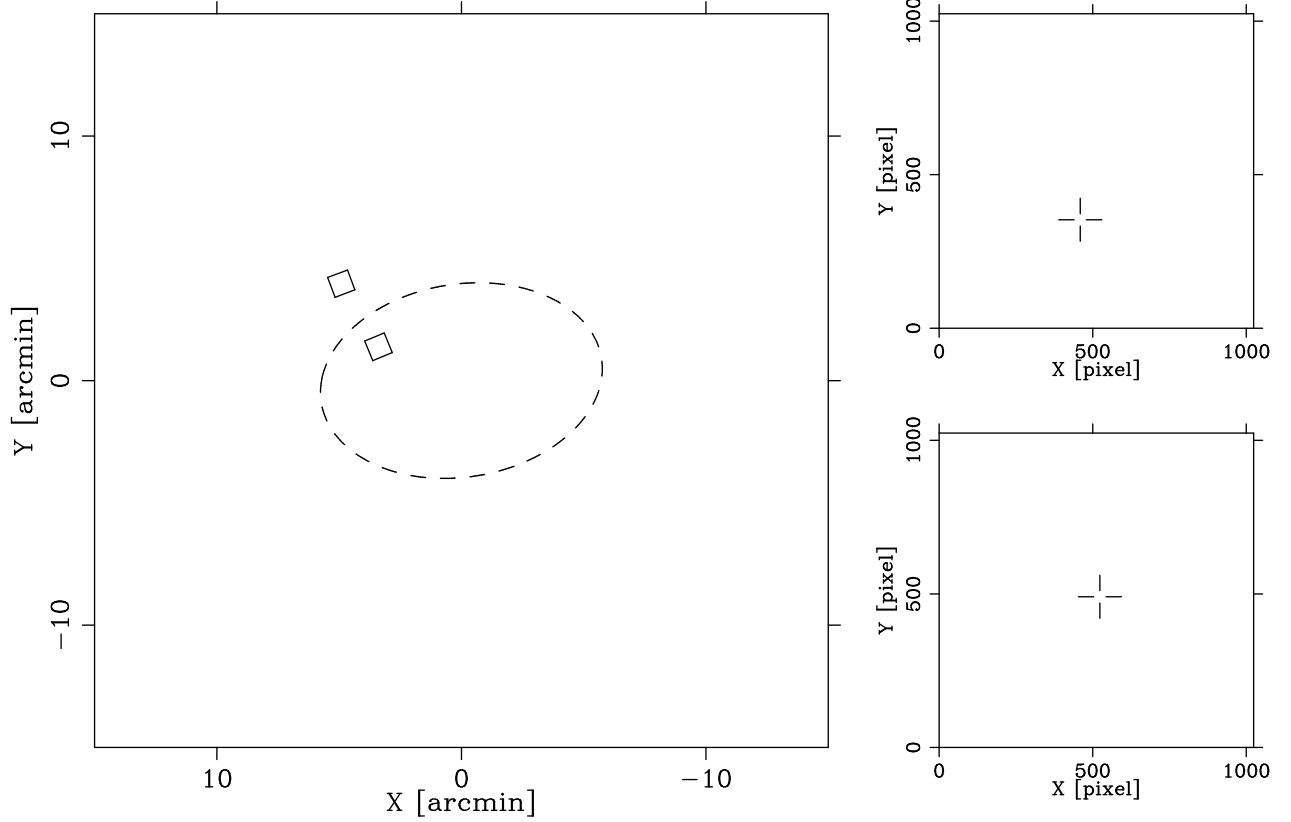


Fig. 1.— Left panel: An image of the sky in the direction of the Sculptor dSph. The dashed ellipse has an ellipticity of 0.32 and a semi-major axis equal to the Irwin & Hatzidimitriou (1995) core radius. The two squares represent the fields studied in this article. The one within the core corresponds to the SCL J0100 – 3341 field and the one outside to the SCL J0100 – 3338 field. Top-right panel: A sample image from the epoch 2000 data for the SCL J0100 – 3341 field. The cross-hair indicates the location of the QSO. Bottom-right panel: A sample image from the epoch 1999 data for the SCL J0100 – 3338 field. Again, the cross-hair indicates the location of the QSO.

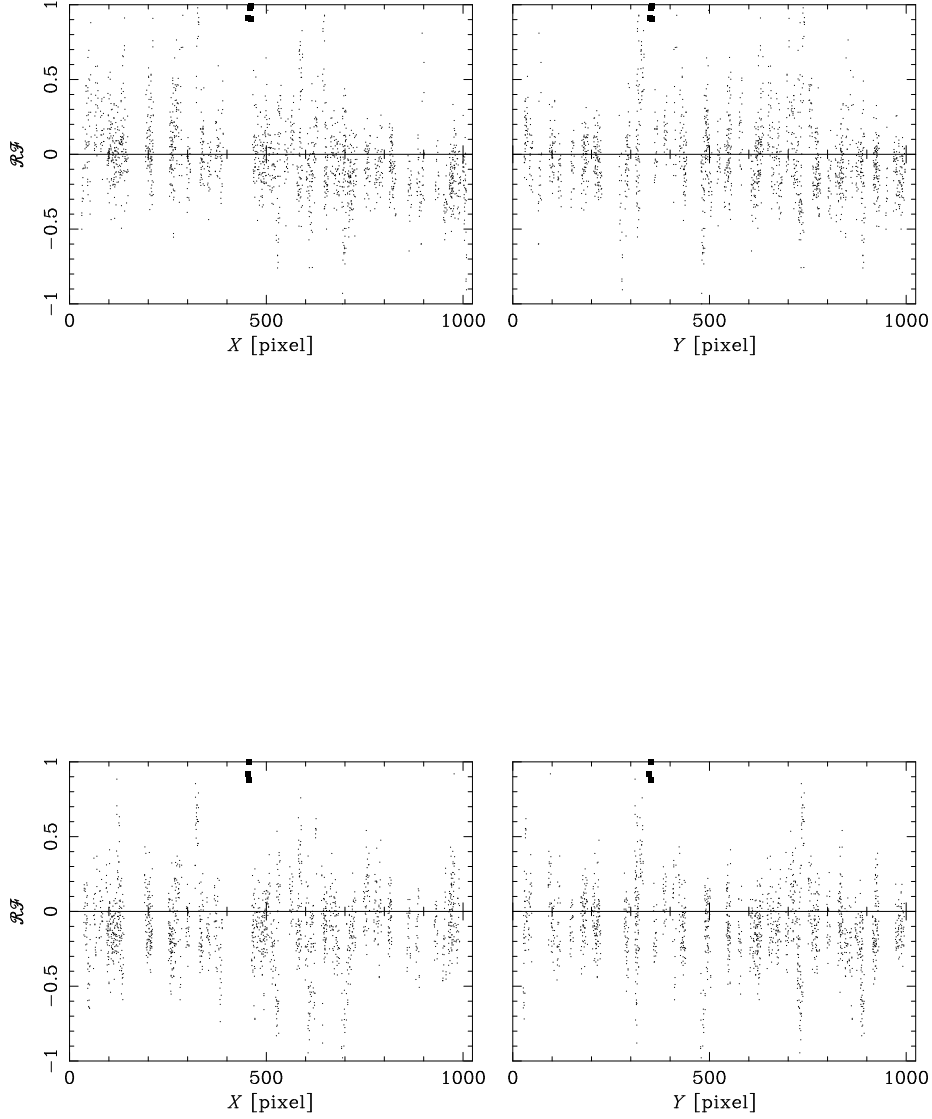


Fig. 2.— Flux residual *versus* location for objects in an image for the SCL  $J0100 - 3341$  field. Every plot displays points from 24 images. The left-hand panels plot  $\mathcal{R}\mathcal{F}$  *versus* the  $X$ -coordinate and the right-hand panels plot  $\mathcal{R}\mathcal{F}$  *versus* the  $Y$ -coordinate. The filled squares represent the QSO. The top row of panels corresponds to the 2000 epoch and the bottom row to the 2002 epoch. For ease of comparison, all of the plots have the same scale on the vertical axis. Only objects with a  $S/N$  greater than 30 are plotted.

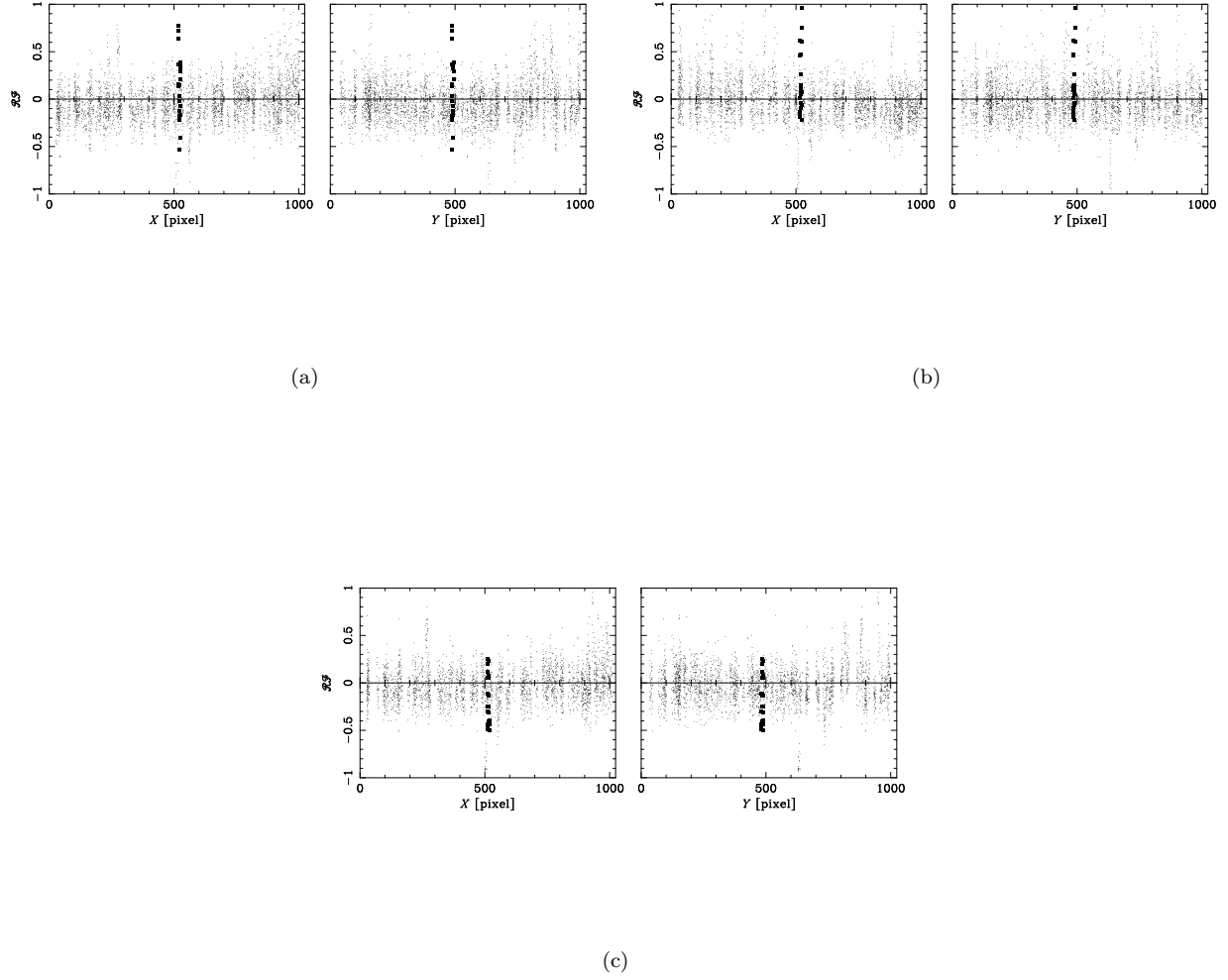


Fig. 3.— Flux residual *versus* location for objects in an image for the SCL J0100 – 3338 field. Every plot displays points from 24 images. The left-hand panels plot  $\mathcal{RF}$  *versus* the  $X$ -coordinate and the right-hand panels plot  $\mathcal{RF}$  *versus* the  $Y$ -coordinate. The filled squares represent the QSO. From top to bottom, the three rows of panels correspond to the 1999, 2000, and 2002 epoch, respectively. For ease of comparison, all of the plots have the same scale on the vertical axis. Only objects with a  $S/N$  greater than 15 are plotted.



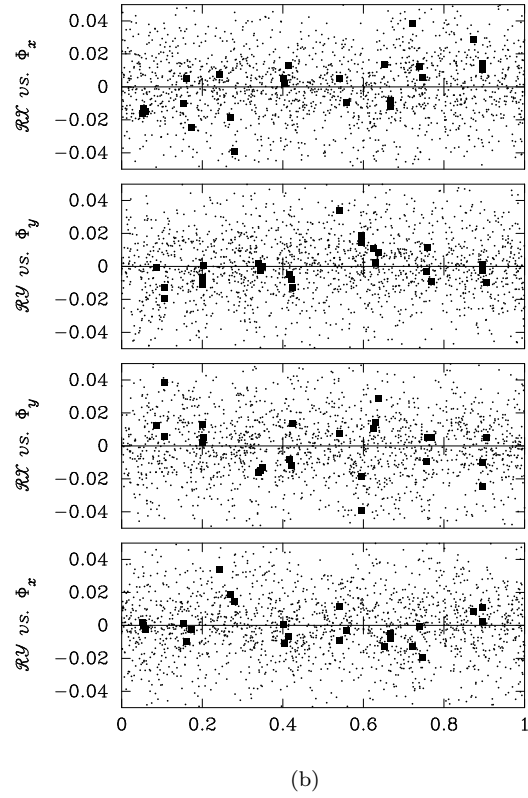
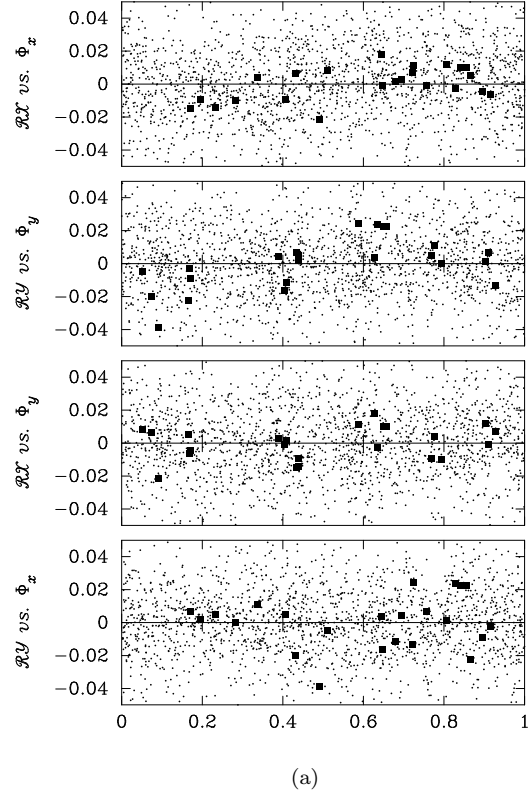


Fig. 4.— Plots for the SCL *J0100 – 3341* field of the position residuals,  $\mathcal{RX}$  and  $\mathcal{RY}$ , as a function of the pixel phase,  $\Phi_x$  and  $\Phi_y$ . The panels a) and b) correspond to the epochs 2000 and 2002, respectively. The filled squares corresponds to the OSO. Only objects with a  $S/N$  greater than 20 are plotted.

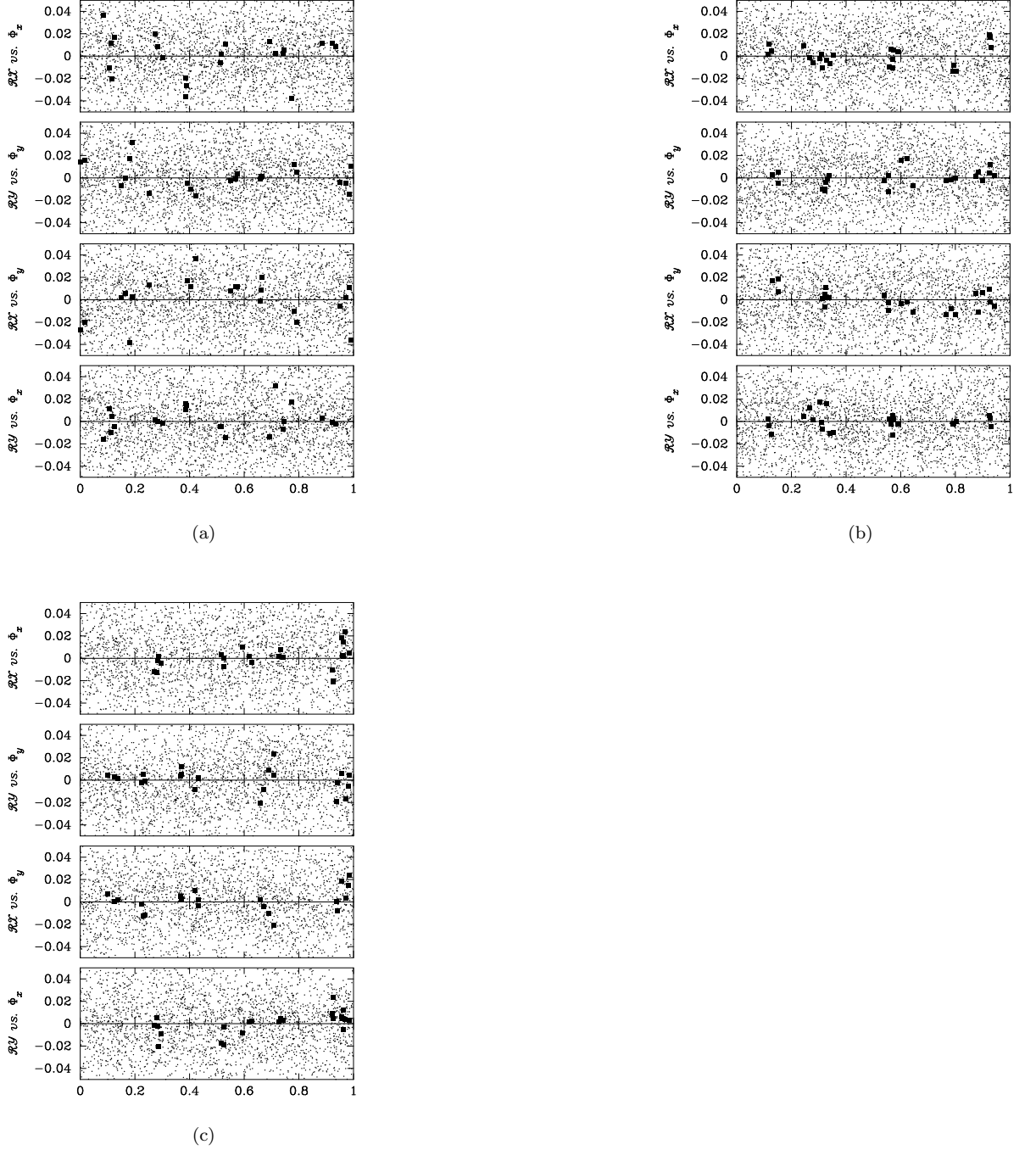


Fig. 5.— Plots for the SCL J0100–3338 field of the position residuals,  $\mathcal{RX}$  and  $\mathcal{RY}$ , as a function of the pixel phase,  $\Phi_x$  and  $\Phi_y$ . The panels a), b), and c) correspond to the epochs 1999, 2000, and 2002, respectively. The filled squares corresponds to the QSO. Only objects with a  $S/N$  greater than 15 are plotted.

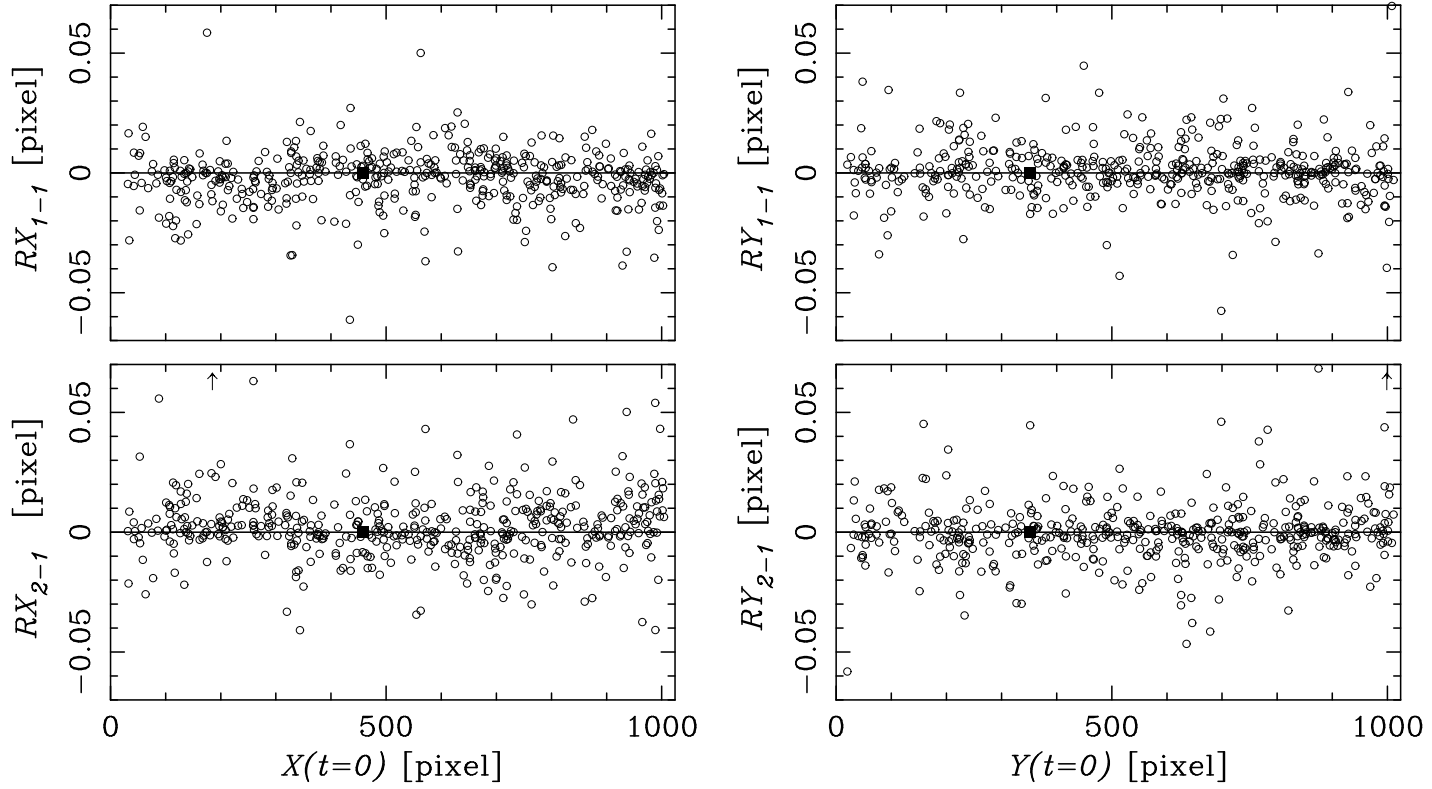


Fig. 6.— Position residuals defined by the Equations 10 and 11 in P05 for the objects in the SCL *J0100–3341* field. From top to bottom, the panels are for the 2000 and 2002 epoch, respectively. The panels on the left show  $RX$  versus  $X$  and those on the right show  $RY$  versus  $Y$ . The filled squares correspond to the QSO. The arrows indicate points beyond the boundaries of the plot. Note the “steps” in the plots of  $RX_{1-1}$  and  $RX_{2-1}$  versus  $X$  at  $X \simeq 320$  pixels.

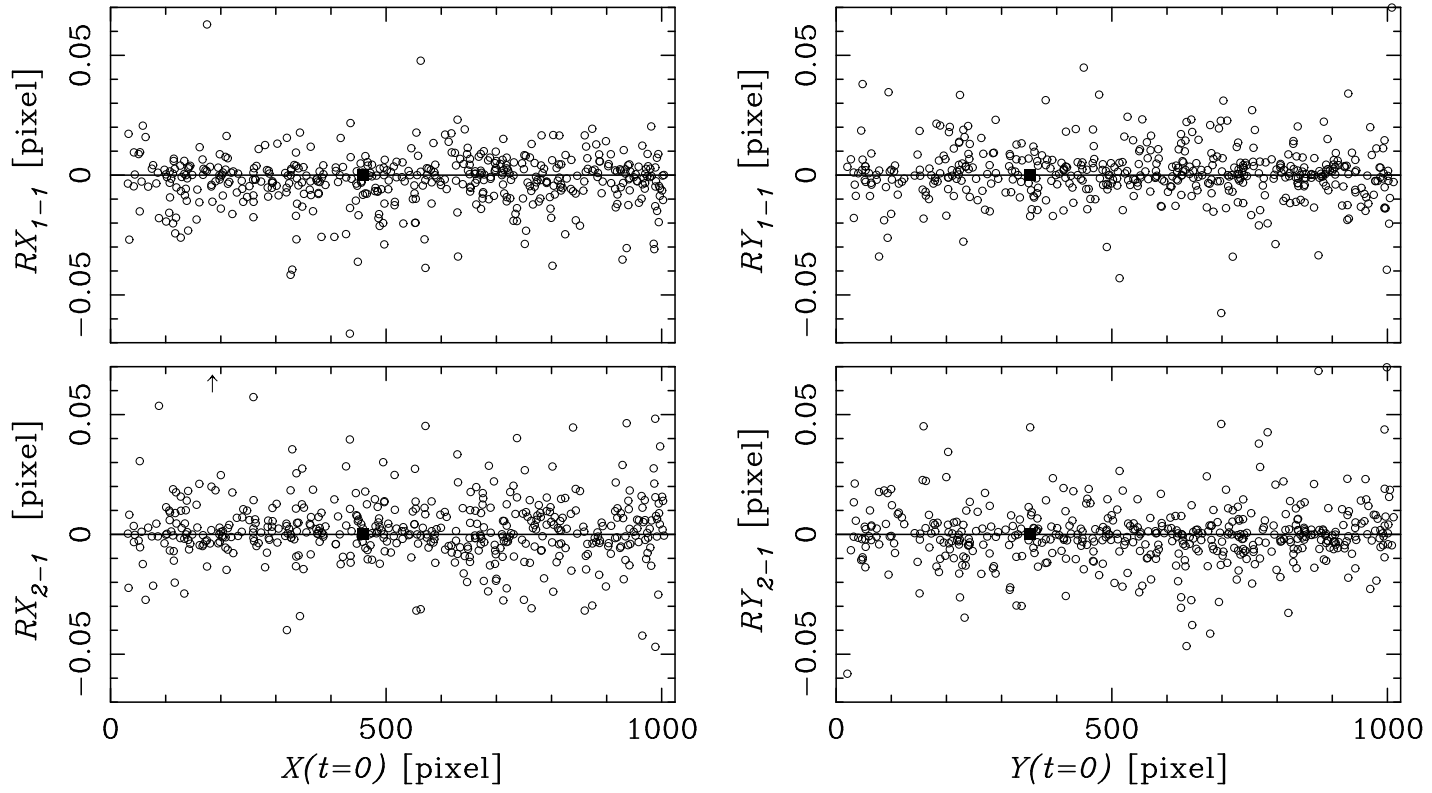


Fig. 7.— The same as Figure 6 after replacing  $x_j^i$  with  $x_j^i + c_7$  in the transformation for  $X \leq 320$  pixels. The fitted value of  $c_7$  is 0.019 pixel. Note the absence of “steps.”

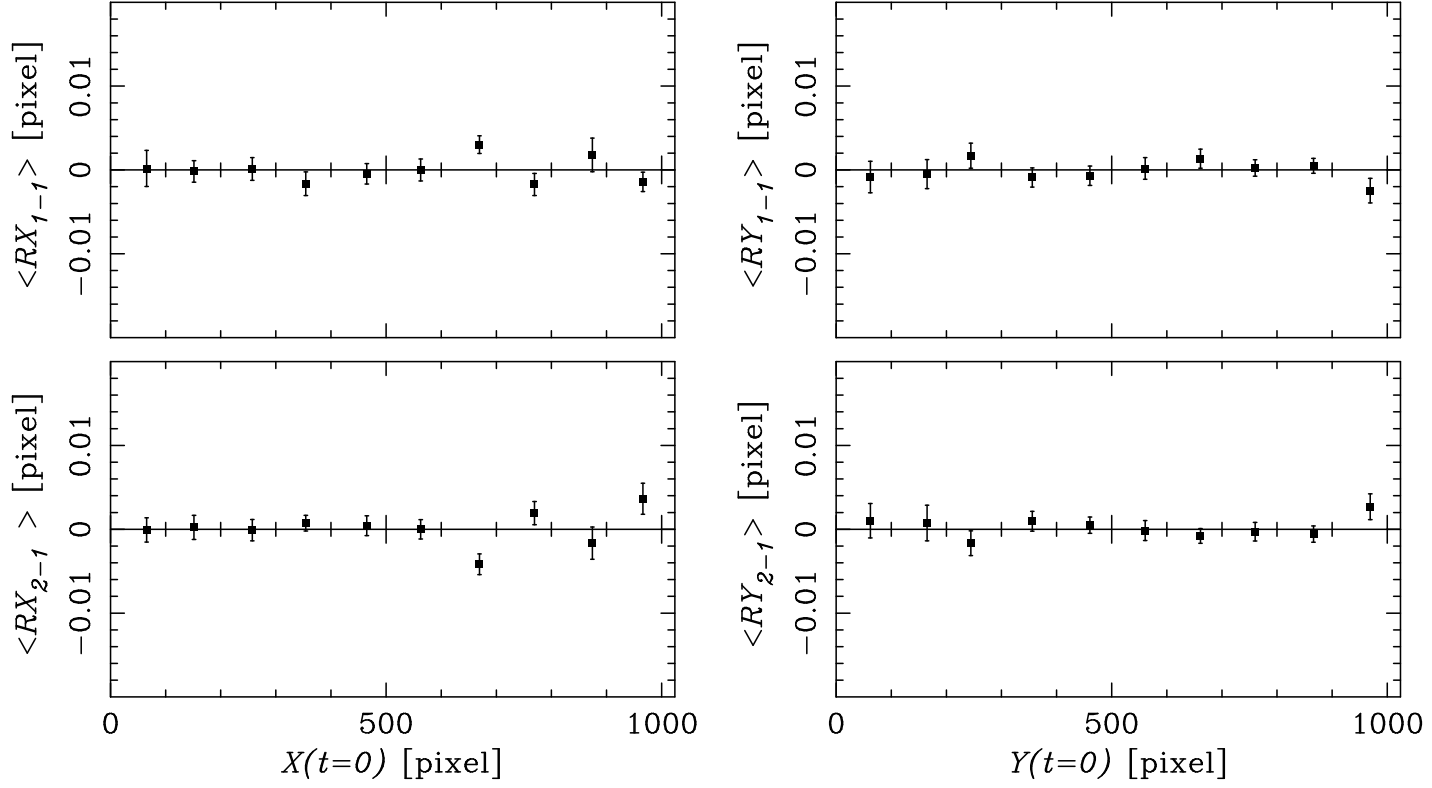


Fig. 8.— The same as Figure 7 except that the points are the weighted mean residuals in ten equal-length bins in  $X$  or  $Y$ . The points are plotted at the mean of the coordinate values in the bin.

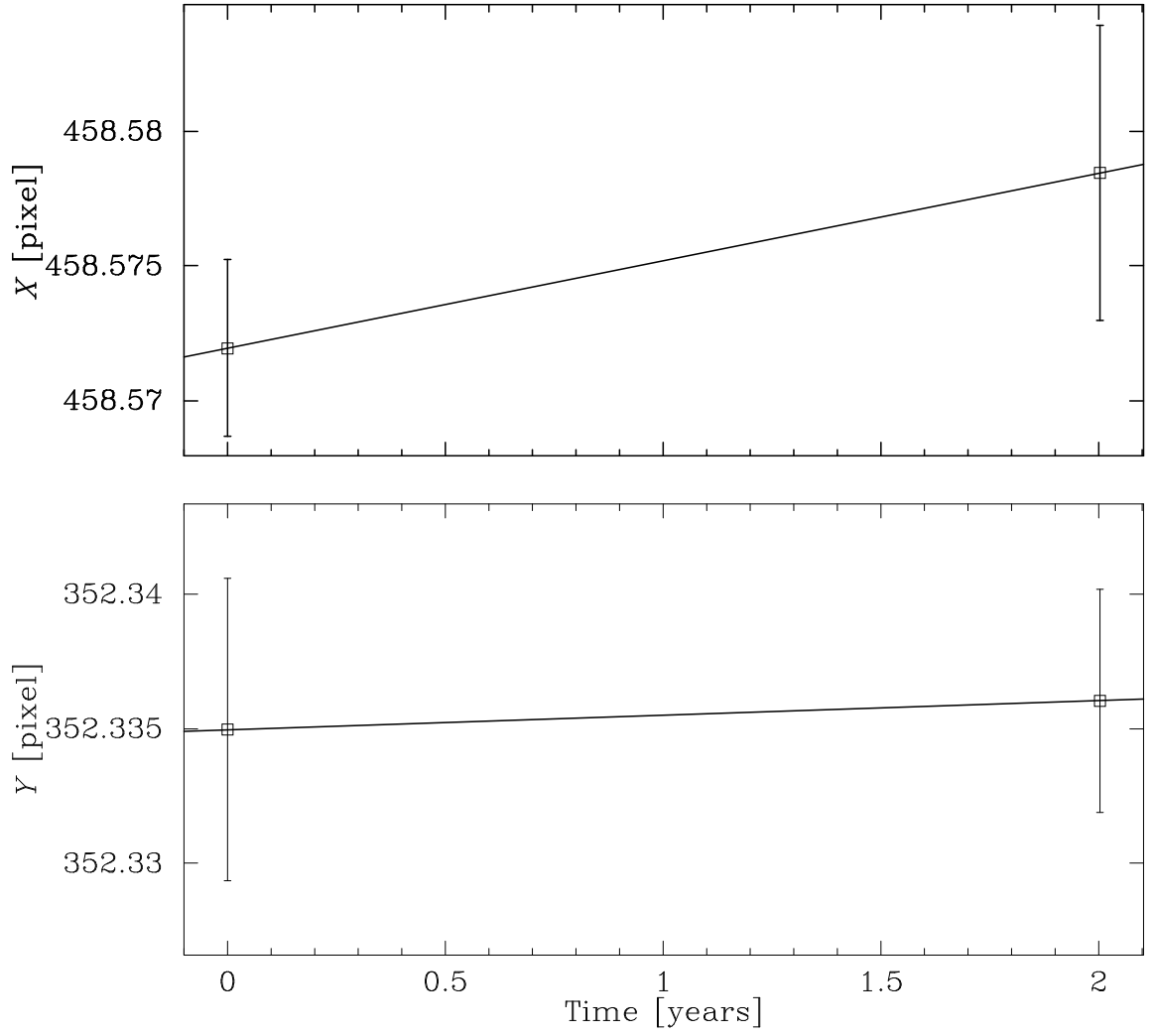


Fig. 9.— The location of the QSO as a function of time for the SCL  $J0100 - 3341$  field in the standard coordinate system. The vertical axis in each plot has the same scale.

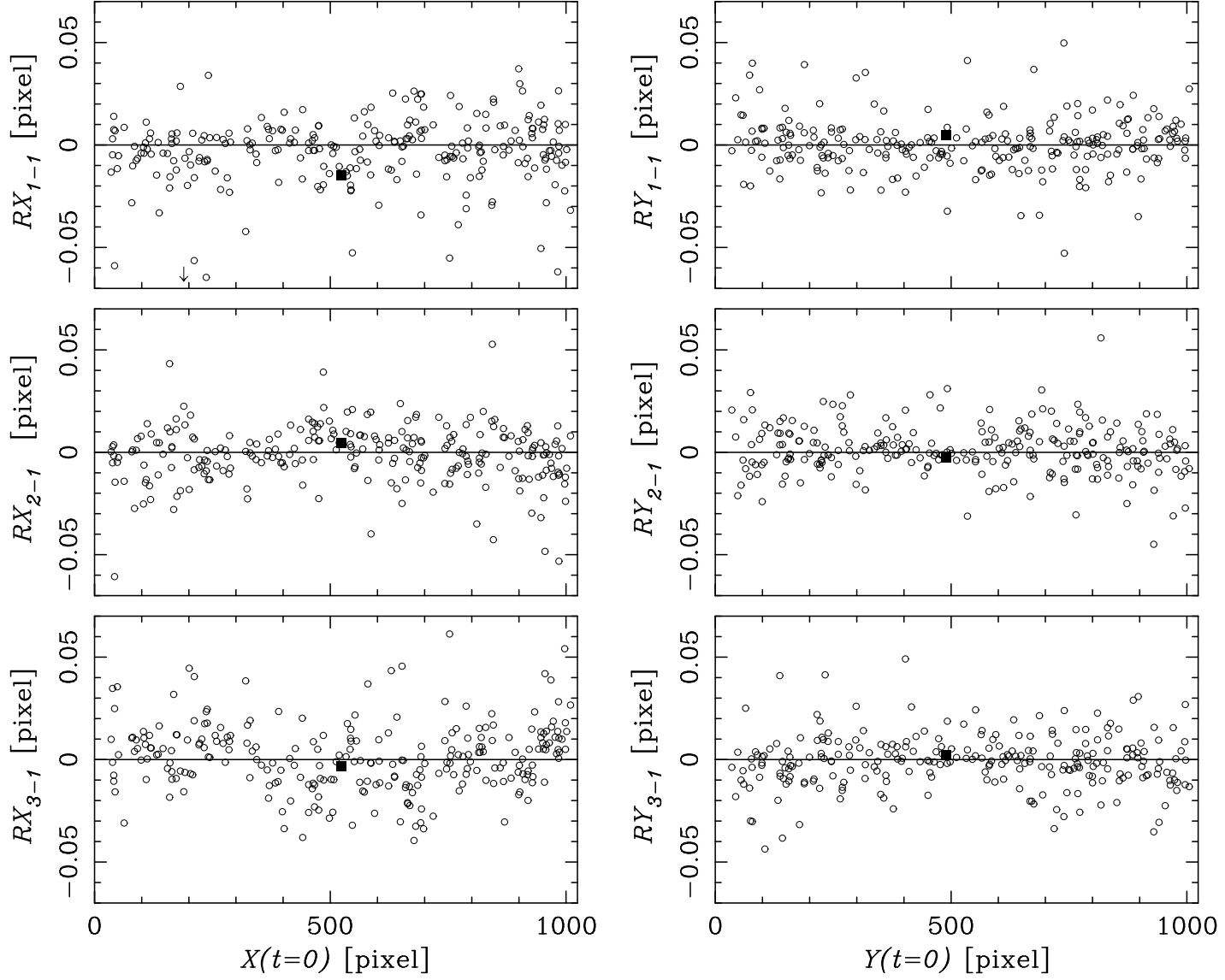


Fig. 10.— Plots of the position residuals for the SCL J0100 – 3338 field. The panels in the left column show  $RX$  versus  $X$  and those in the right column show  $RY$  versus  $Y$ . The epochs increase chronologically from the top to the bottom row. The filled squares mark the QSO. The arrow indicates a point beyond the boundaries of the plot.

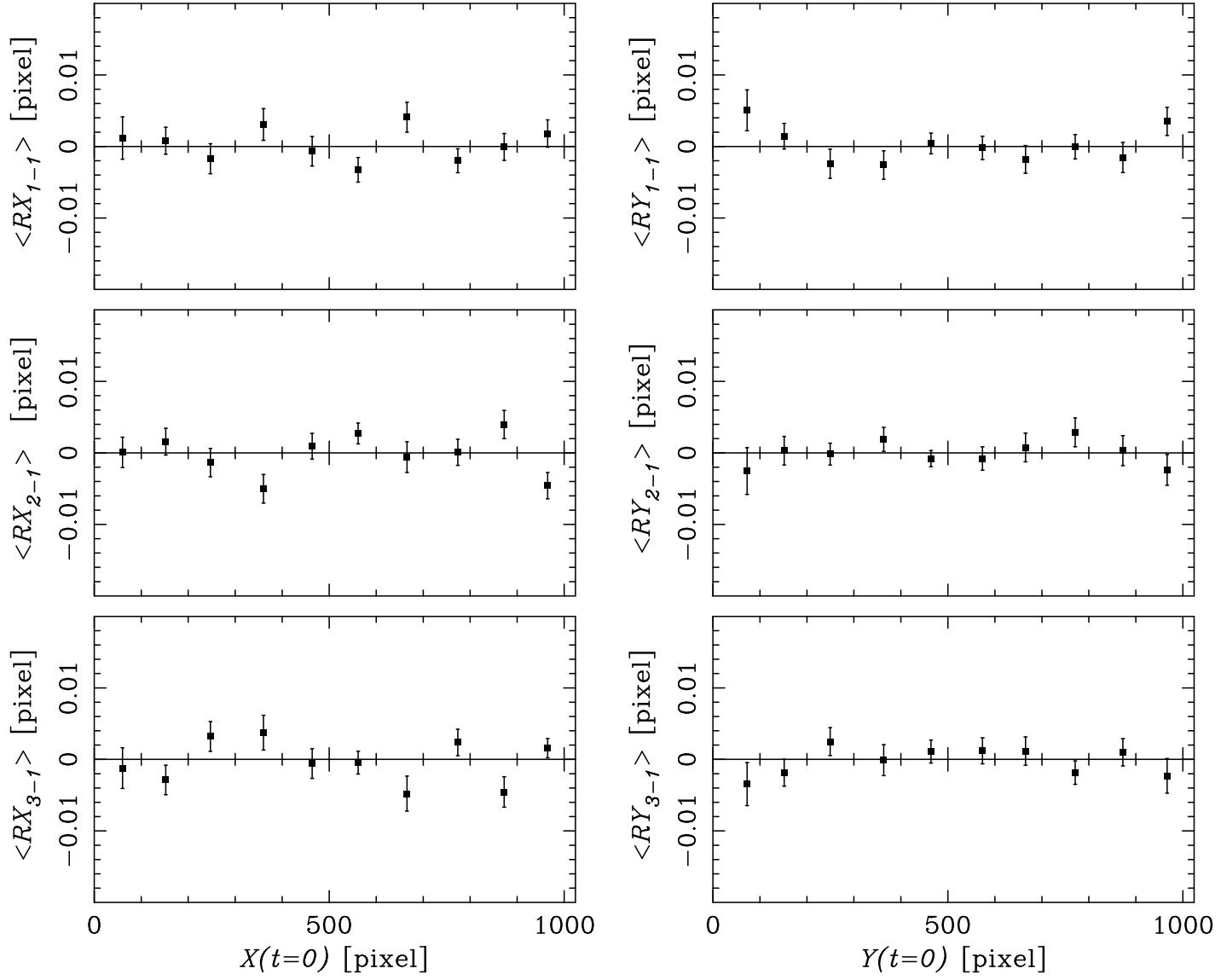


Fig. 11.— The same as Figure 10 except that the points are the weighted mean residuals in ten equal-length bins in  $X$  or  $Y$ . The points are plotted at the mean of the coordinate values in the bin.



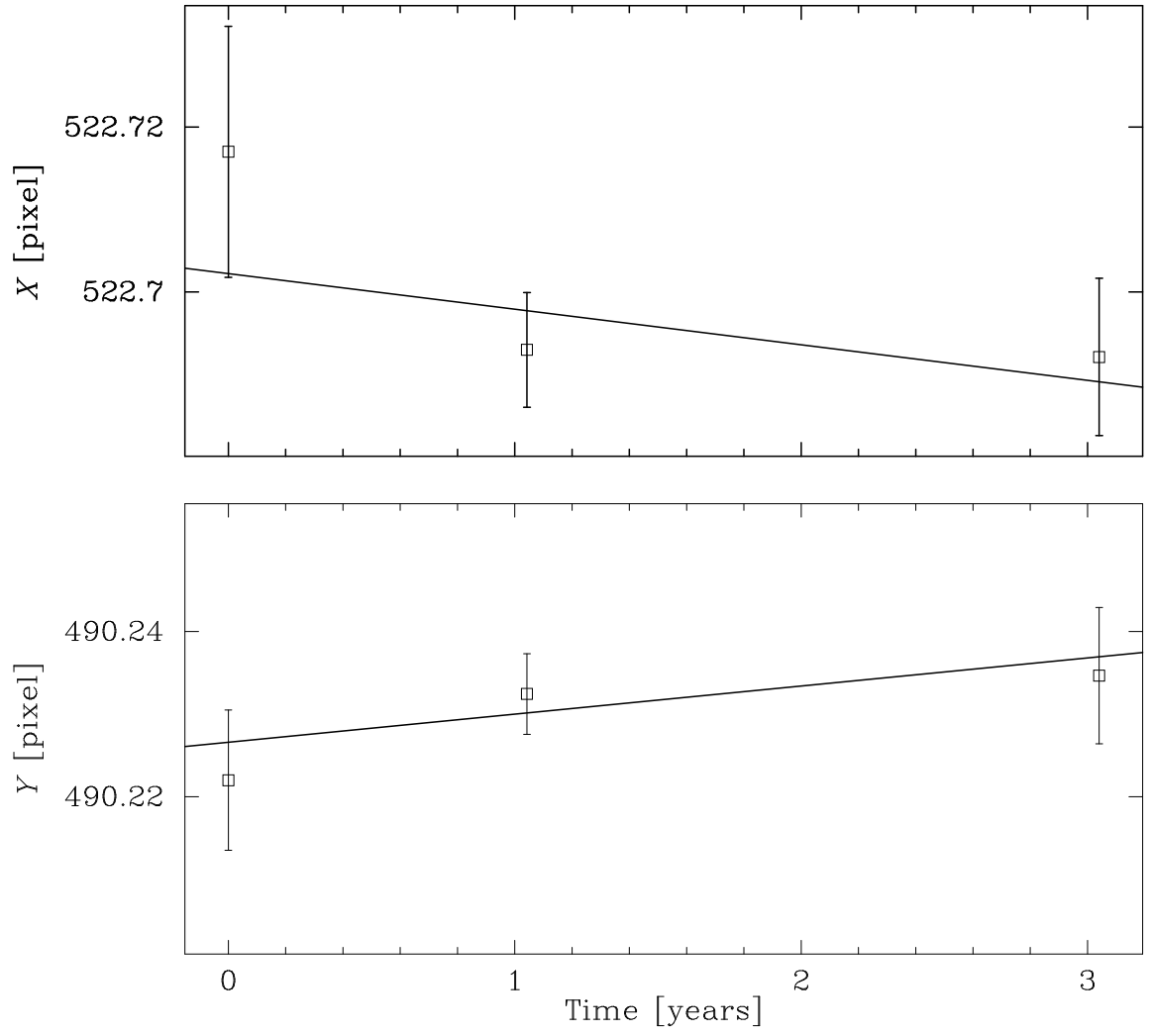


Fig. 12.— The location of the QSO as a function of time for the SCL *J0100 – 3338* field in the standard coordinate system. The vertical axis in each plot has the same scale.

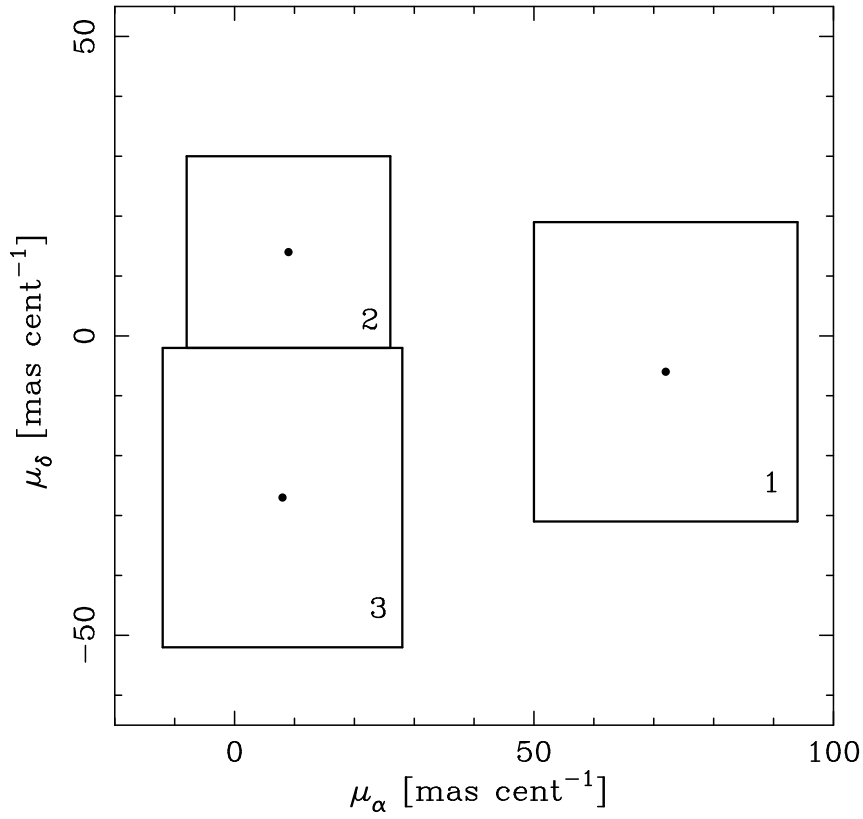


Fig. 13.— Comparison of three independent measurements of the proper motion for Sculptor. The center of a rectangle — marked with a dot — is the best estimate of the proper motion and the sides are offset by the  $1\text{-}\sigma$  uncertainties. Rectangles 1, 2, and 3 correspond to the measurements from Schweitzer et al. (1995), this study (field SCL *J0100 – 3341*), and this study (field SCL *J0100 – 3338*), respectively.

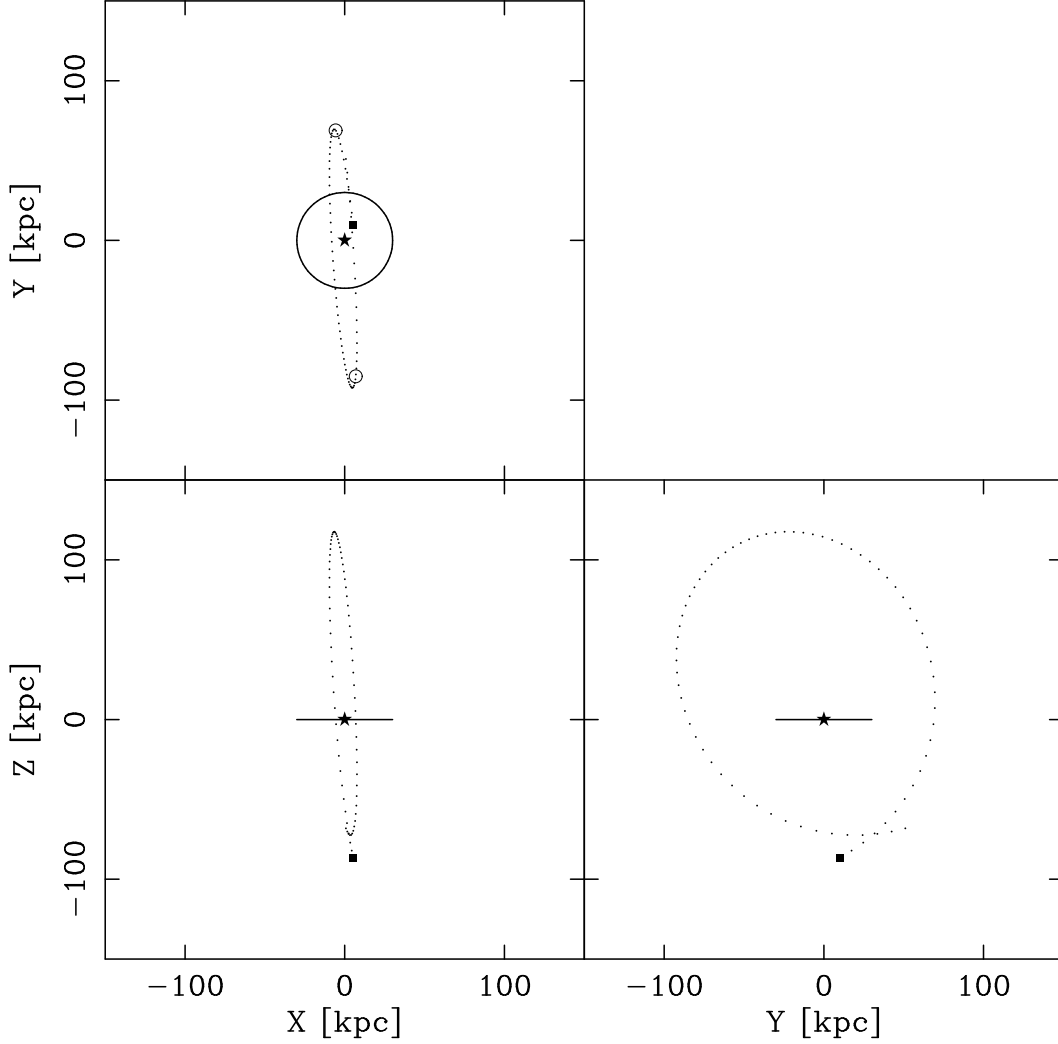


Fig. 14.— Projections of the orbit of Sculptor onto the  $X - Y$  plane (top-left panel), the  $X - Z$  plane (bottom-left panel), and the  $Y - Z$  plane (bottom-right panel). The origin of the right-handed coordinate system is at the Galactic center, which is marked with a filled star. The Galactic disk is in the  $X - Y$  plane and the present location of the Sun is on the positive  $X$  axis. The filled square marks the current location of Sculptor at  $(X, Y, Z) = (5.4, 9.9, -86)$  kpc. For reference, the large circle in the  $X - Y$  plane has a radius of 30 kpc. The three small circles in the  $X - Y$  projection mark the points where Sculptor passes through the plane of the Galactic disk. The integration starts from the present and extends backwards in time for 3 Gyr.

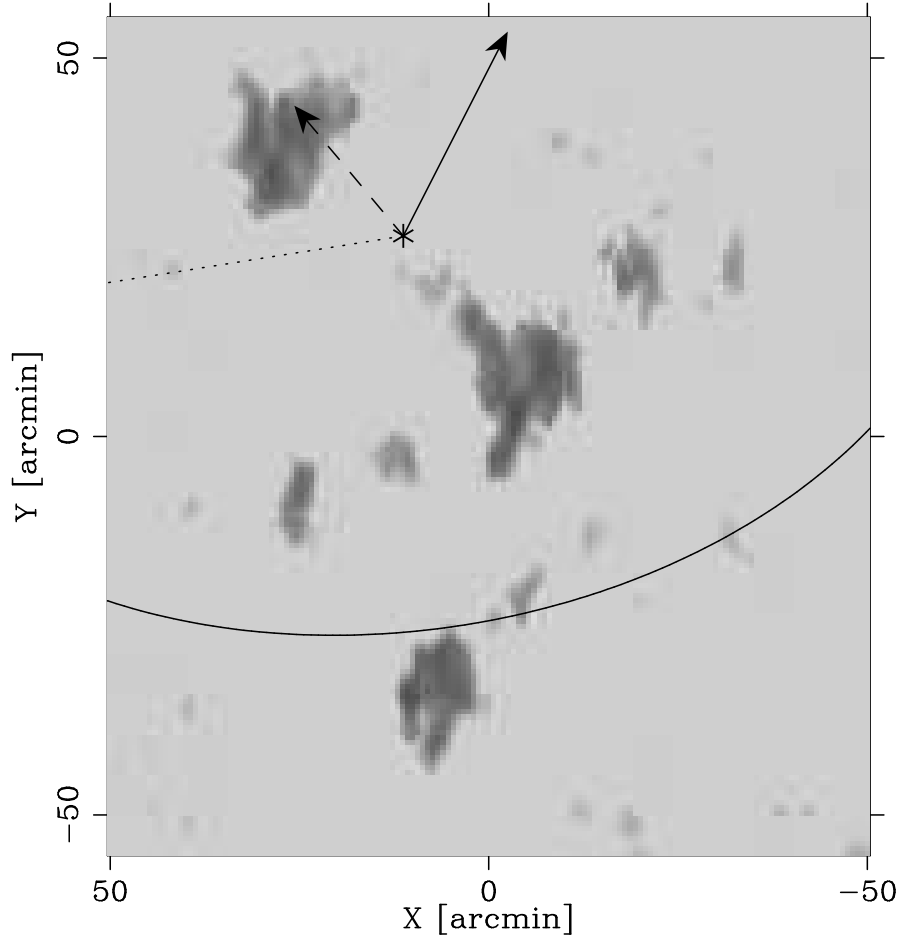


Fig. 15.— *Gray-scale map:* The distribution of HI in the direction of Sculptor based on data taken with the Australia Telescope Compact Array by Bouchard et al. (2003). The map is centered at  $(X, Y) = (0, 0)$ , which corresponds to  $(\alpha, \delta) = (00^{\text{h}}59^{\text{m}}18^{\text{s}}, -34^{\circ}10'00'')$  (J2000.0). North is up and East is to the left. Overplotted on the map are: the center of Sculptor (asterisk); its optical boundary (ellipse); the galactic rest frame proper motion derived by Schweitzer et al. (1995) (dashed arrow) and by us (solid arrow); and the line connecting the centers of Sculptor and Fornax (dotted line).

Table 1. Measured Proper Motion of Sculptor

Field (1)	$\mu_\alpha$ (mas cent <sup>-1</sup> ) (2)	$\mu_\delta$ (mas cent <sup>-1</sup> ) (3)
SCL J0100 – 3341	$9 \pm 17$	$14 \pm 16$
SCL J0100 – 3338	$8 \pm 20$	$-27 \pm 25$
Weighted mean	$9 \pm 13$	$2 \pm 13$

Table 2. Measured Proper Motions For Objects in the SCL J0100 – 3341 Field

ID (1)	X (pixels) (2)	Y (pixels) (3)	$S/N$ (4)	$\mu_\alpha$ (mas cent <sup>-1</sup> ) (5)	$\mu_\delta$ (mas cent <sup>-1</sup> ) (6)	$\chi^2$ (7)
1	459	352	125	$0 \pm 21$	$0 \pm 21$	...
2	327	740	164	$2766 \pm 17$	$1048 \pm 18$	...
3	588	330	112	$-812 \pm 16$	$-1714 \pm 17$	...
4	137	627	99	$180 \pm 17$	$-127 \pm 21$	...
5	496	398	10	$-66 \pm 46$	$178 \pm 72$	...
6	574	710	6	$36 \pm 93$	$258 \pm 63$	...

Table 3. Measured Proper Motions For Objects in the SCL J0100 – 3338 Field

ID (1)	X (pixels) (2)	Y (pixels) (3)	$S/N$ (4)	$\mu_\alpha$ (mas cent <sup>-1</sup> ) (5)	$\mu_\delta$ (mas cent <sup>-1</sup> ) (6)	$\chi^2$ (7)
1	523	490	180	$0 \pm 24$	$0 \pm 28$	2.10
2	414	177	42	$-188 \pm 22$	$-299 \pm 20$	0.61
3	950	832	20	$89 \pm 31$	$-562 \pm 27$	4.25

Table 4. Galactic-Rest-Frame Proper Motion and Space Velocity of Sculptor

Field (1)	$\mu_\alpha^{\text{Grf}}$ (mas cent <sup>-1</sup> ) (2)	$\mu_\delta^{\text{Grf}}$ (mas cent <sup>-1</sup> ) (3)	$\mu_l^{\text{Grf}}$ (mas cent <sup>-1</sup> ) (4)	$\mu_b^{\text{Grf}}$ (mas cent <sup>-1</sup> ) (5)	$\Pi$ (km s <sup>-1</sup> ) (6)	$\Theta$ (km s <sup>-1</sup> ) (7)	$Z$ (km s <sup>-1</sup> ) (8)	$V_r$ (km s <sup>-1</sup> ) (9)	$V_t$ (km s <sup>-1</sup> ) (10)
SCL J0100 – 3341	$-23 \pm 17$	$57 \pm 16$	$6 \pm 17$	$-62 \pm 17$	$-186 \pm 69$	$159 \pm 68$	$-107 \pm 8$	$82 \pm 7$	$254 \pm 66$
SCL J0100 – 3338	$-24 \pm 20$	$17 \pm 25$	$18 \pm 21$	$-23 \pm 25$	$-113 \pm 88$	$10 \pm 100$	$-88 \pm 12$	$73 \pm 9$	$124 \pm 76$
Weighted mean	$-23 \pm 13$	$45 \pm 13$	$11 \pm 13$	$-50 \pm 14$	$-158 \pm 54$	$112 \pm 56$	$-101 \pm 7$	$79 \pm 6$	$198 \pm 50$

Table 5. Orbital elements of Sculptor

Quantity (1)	Symbol (2)	Unit (3)	Value (4)	95% Conf. Interv. (5)
Perigalacticon	$R_p$	kpc	68	(31, 83)
Apogalacticon	$R_a$	kpc	122	(97, 313)
Eccentricity	$e$		0.29	(0.26, 0.60)
Period	$T$	Gyr	2.2	(1.5, 4.9)
Inclination	$\Phi$	deg	86	(83, 90)
Longitude	$\Omega$	deg	275	(243, 306)

Table 6. Predicted Proper Motion of Sculptor

Stream No. (1)	$\mu_\alpha$ (2)	$\mu_\delta$ (3)	$ \vec{\mu} $ (4)	PA (degrees) (5)
	(mas cent <sup>-1</sup> )			
2	51	−80	95	147
4a	80	−61	101	127
4b	−13	−27	30	205
Our Result	$9 \pm 13$	$2 \pm 13$	$9 \pm 13$	$77 \pm 81$